ACSNANO
www.acsnano.org
ARTICLE

Epitaxy-Induced Assembly and Enantiomeric Switching of an On-Surface Formed Dinuclear Organocobalt Complex

Raphael Hellwig,[†] Tobias Paintner,[†] Zhi Chen,[‡] Mario Ruben,[‡,¶] Ari Paavo Seitsonen,[§] Florian Klappenberger,[*,†] Harald Brune,[∥,⊥] and Johannes V. Barth[†]

[†]Physik Department E20, Technische Universität München, Garching D-85748, Germany
[‡]Institute of Nanotechnology, Karlsruhe Institute of Technology, Eggenstein-Leopoldshafen D-76344, Germany
[¶]Institute de Physique et Chimie de Matériaux de Strasbourg (IPCMS), CNRS-Université de Strasbourg, Strasbourg F-67034, France
[§]Département de Chimie, Ecole Normale Supérieure (ENS), Paris Cedex 05 F-75230, France
[∥]Institute of Physics, Ecole Polytechnique Fédérale de Lausanne (EPFL), Station 3, Lausanne CH-1015, Switzerland
[⊥]Institute for Advanced Study (TUM-IAS), Lichtenbergstr. 2a, Garching D-85748, Germany

Supporting Information

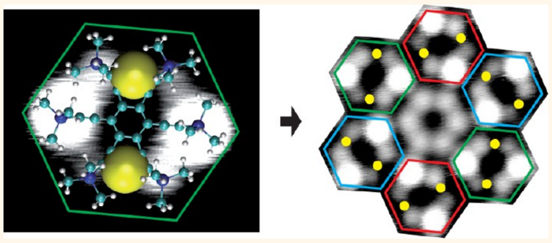

ABSTRACT: **We report on the surface-guided synthesis of a dinuclear organocobalt complex, its self-assembly into a complex nanoarchitecture, and a single-molecule level investigation of its switching behavior. Initially, an organic layer is prepared by depositing hexakis((trimethylsilyl)ethynyl)-benzene under ultra-high-vacuum conditions onto Ag(111). After Co dosage at 200 K, low-temperature scanning tunneling microscopy (STM) reveals an epitaxy-mediated organization mechanism of molecules and on-surface formed organometallic complexes. The dinuclear complexes contain two bis(η^2-alkynyl) π-tweezer motifs, each stabilizing a single Co atom and express two enantiomers due to a conformation twist. The chirality is transferred to the two-dimensional architecture, whereby its Co adatoms are located at the corners of a 3.4.6.4 rhombitrihexagonal tessellation due to the systematic arrangement and anchoring of the complexes. Extensive density functional theory simulations support our interpretation of an epitaxy-guided surface tessellation and its chiral character. Additionally, STM tip-assisted manipulation experiments on isolated dinuclear complexes reveal controlled and reversible switching between the enantiomeric states *via* inelastic electron processes. After activation by bias pulses, structurally modified complexes display a distinctive Kondo feature attributed to metastable Co configurations.**

KEYWORDS: *cobalt alkynyl complex, surface tessellation, single-molecule switch, scanning tunneling microscopy*

The rational design and synthesis of 2D-confined functional nanoarchitectures of well-defined optic, magnetic, and catalytic properties remain one of the key challenges toward the realization of future nanotechnology.[1−6] When targeting the controlled fabrication and embedding of magnetic nanoobjects, such as single atoms,[7] small clusters,[8] or single-molecule magnets,[9] stepwise bottom-up construction *via* templates under ultrahigh-vacuum (UHV) conditions provides a versatile route. One-atom thick sheets of graphene and boron nitride proved to be suitable templates for the trapping of metallic clusters[10−14] at specific sites of the substrate-related Moiré lattices. Open-porous metal−organic coordination networks[15] were employed for the selective decoration with transition-metal clusters[16] and the confinement of single atoms.[17] A self-assembled and highly ordered layer of diphenyl oxalic amide molecules was used to selectively bind monomeric cobalt on top of benzene rings, thereby establishing a well-ordered Co superlattice.[18]

Metal alkynyl complexes[19] are attractive for various research fields, such as non-linear optics,[20] intramolecular charge transfer systems,[21] and photovoltaics.[22] Moreover, they constitute the key building block for metallopolymers, an emerging class of functional soft materials.[23]

Despite their importance for functional materials, insight on interfacial alkynyl complexes is scarce, but a handful of first results demonstrate interesting prospects. Liu *et al.* reported the formation of surface-guided molecular wires stabilized by Ag-bisalkynyl coordination.[24] Polyyne-coupled dinuclear complexes proved that mixed valence state chemistry is operational

Received: September 9, 2016
Accepted: January 18, 2017
Published: January 18, 2017

DOI: 10.1021/acsnano.6b06114
ACS Nano 2017, 11, 1347−1359

on metallic surfaces.[25,26] Ni−alkyne bonding facilitated the post-functionalization of an adaptable metal−organic network.[27]

Recently, we reported the surface-guided formation of an original organocobalt complex from a precursor with one internal alkyne moiety. The established organometallic compound holds no counterpart in solution chemistry highlighting the intriguing phenomena triggered by the interfacial conditions.[28] Related organocobalt structures are highly relevant for chemical research and the development of synthesis protocols, where organocobalt compounds represent indispensable ingredients for numerous synthesis pathways based on the Pauson−Khand and Nicholas reaction and also the hydroformylation reaction.[29]

Here, we investigated an organic species with six internal alkynes, thus bearing multiple organometallic binding sites. Exposing an organic template of self-assembled hexakis-((trimethylsilyl)ethynyl)benzene (HEB) molecules on Ag(111) to a beam of single Co atoms leads to the formation of mononuclear (C_1) and dinuclear organocobalt complexes (C_2), which arrange in a highly ordered two-dimensional (2D) nanoarchitecture representing a 3.4.6.4 tiling pattern. Utilizing the combination of high-resolution scanning tunneling microscopy (STM) and state-of-the-art density functional theory (DFT) modeling, we elucidate the structure of complexes and the intriguing surface tessellation. The chiral dinuclear complexes contain two bis(η^2-alkynyl) π-tweezer motifs,[30,31] each stabilizing a single Co atom in a geometry that contrasts the more common scenario of σ-like metal−carbon bonding within alkynyl complexes.[19]

Furthermore, *via* a single-molecule level investigation of isolated C_2, we achieved well-controlled and reversible two-state switching between chiral isomers attributed to conformational changes and demonstrate the appearance of a Kondo signature after tip-induced modification of the complex.

RESULTS AND DISCUSSION

Organic Layer. Within this study, we use the *de novo* synthesized six-fold symmetric alkyne derivative HEB (see Supporting Information (SI) and Figure S1 for synthetic details) with stochiometric formula $C_{36}Si_6H_{54}$. According to Figure 1a, the chemical structure is comprised of a central arene ring connected to six internal alkynes, each terminated by a trimethylsilyl group (TMS). Figure 1b−d shows different perspectives of a ball-and-stick molecular model established by geometry optimization *via* gas-phase DFT calculations. The calculated distances between adjacent alkynes are shown in the top view of the molecule (Figure 1c), the alkyne's bending flexibility is indicated by the out-of-plane (in-plane) angle ε (φ) (Figure 1b,c), and free rotations of the TMS groups around σ bonds are indicated by the angle γ (Figure 1d). The mutual orientations of the six TMS groups induce chirality within surface-adsorbed molecules.

In a first step, the chemical vapor deposition (CVD) of HEB on the clean Ag(111) surface, kept at 450 K and in an UHV environment, was performed in order to grow a sub-ML molecular interface (see Figure S2 for preparation details). After transferring the sample to a LT-STM, the measurements show extended, homogeneous, and largely defect-free organic layers (Figure 2a), indicative of a high molecular mobility and weak intermolecular interactions allowing structural autocorrection mechanisms during the self-assembly process. The hexagonal symmetry and dense packing scheme of the islands is rationalized by the predominance of attractive van der Waals interactions between bulky TMS end groups, leading to relatively weak molecular cohesion and adhesion, consistent with manipulation experiments (see Figure S2e). When superimposing a Ag(111) lattice model and molecular models to high-resolution STM data (Figure 2b), the six bright lobes surrounding a central void coincide with the six TMS-alkyne groups. Based on high-resolution STM imaging and the absence of Moiré-like effects in the STM contrast, we tentatively suggest a commensurate $\sqrt{31} \times \sqrt{31}$ R 8.9° adsorption structure, which reads in matrix notation:

$$\begin{pmatrix} \vec{a} \\ \vec{b} \end{pmatrix} = \begin{pmatrix} 6 & -1 \\ 1 & 5 \end{pmatrix} \begin{pmatrix} \vec{u} \\ \vec{v} \end{pmatrix}$$

where by $\vec{u}$ and $\vec{v}$ are the primitive vectors of Ag(111). As justified in the following analysis of organometallic units within Co-decorated organic islands (*cf.* Figures 2c,d and S3), we tentatively postulate that the molecules' centers adsorb on six-fold symmetric top sites. Besides this domain labeled α, a further domain orientation exists with its unit cell reading in matrix notation: $\begin{pmatrix} 5 & 1 \\ -1 & 6 \end{pmatrix}$, as shown in Figure 2c. The existence of this domain β is rationalized by a combination of the molecule's six-fold symmetry and alignment with respect to a crystallographic symmetry axis. A hexagonal contour enclosing a molecule with an associated line along opposite molecular lobes (Figure 2b,c) reveals that the orientation of the molecules is different in the two domains. We found a rotation of 8° with respect to the three mirror symmetry axes coinciding with the substrate's $\langle 11\bar{2} \rangle$ directions (purple line representing one of them). Therefore, the molecular arrangement is chiral and is expressed in two enantiomorphous domains, which are distinguished by a 16° rotation of the unit cell.

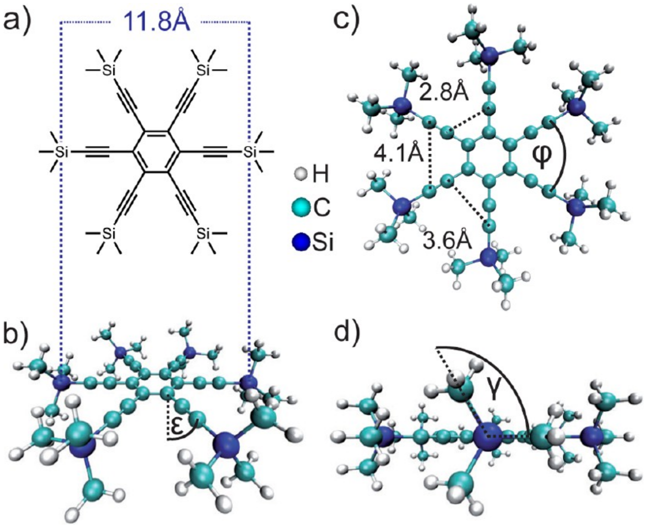

Figure 1. (a) Chemical structure model of HEB. (b) DFT-calculated atomic ball-and-stick visualization of the molecular structure comprised of carbon (cyan), silicon (blue), and hydrogen (white) atoms. (c, d) Top and side view of calculated geometry.

Co Dosage at 12 K. To study the interaction of Co atoms with the organic template in the absence of molecular diffusion, cluster formation, or catalytic reactions, we performed an *in situ* Co dosage with the sample kept in the STM at temperatures below 12 K. Figure 2c presents a β domain decorated with Co,

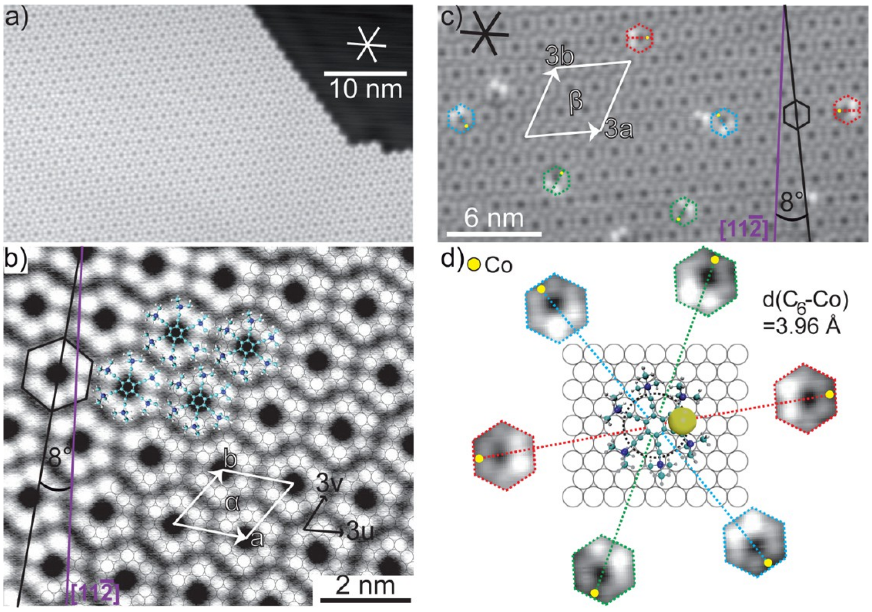

Figure 2. Organic phase showing α (b) and β domains (a,c), which differ by the molecular alignment (black line with outlined molecule). Dense-packed and $[11\bar{2}]$ directions are indicated by stars and purple lines, respectively. (a) Large-scale STM image of a HEB island, and (b) high-resolution image with superimposed unit cell, molecular models, and tentative substrate registry. (c) Co-decoration of organic phase after *in situ* Co dosage at 12 K. Organometallic complexes with marked Co atoms (yellow dots) are color-coded according to their orientation. (d) Gas-phase DFT-calculated geometry of C_1 superimposed on the Ag(111) lattice, and zoomed-in images of the six orientations of C_1 observed in (c). Crossings of dashed circle and dashed lines mark hollow adsorption sites for Co center. Tunneling parameters V_t, I_t: (a, c, d) −100 mV, 100 pA; (b) −10 mV, 49 pA.

where one can observe that the molecular domain structure described above remains preserved, however a new species is present within the matrix of unaltered HEB. This species appears in six different orientations (dashed outline). It is imaged with a characteristic depression on one side and two protruding lobes on the opposite side, and is denoted by C_1. From large-scale STM topographs (see Figure S3a), we determined the coverage of Co in this sample to be approximately 0.002 ML, where one ML corresponds to one Co atom per Ag(111) surface atom. Putting this value in relation with the number of altered molecules, we infer that each C_1 hosts one Co atom. At such low dosage temperatures and Co concentrations, the organic template suppresses Co clustering, while at the same time intramolecular relaxation mediates the formation of the Co-bisalkyne geometry of C_1.

Figure 2d shows high-resolution images of the six different orientations of C_1, which are classified by three colored dashed lines. Interestingly, gas-phase DFT modeling reveals a site-selective interaction between a Co atom and a HEB molecule, hence rationalizing the formation of a C_1 complex incorporating a Co-bis(alkynyl) tweezer-like binding motif. Albeit neglecting unavoidable geometrical adaptations during adsorption, the model helps in explaining the low-symmetry structure of the C_1 appearance in the STM images (see Figure S3b for a side view). The π-tweezer bonding is known for various transition metals[31] and can afford stable interactions.[32] Interestingly, reports on related cobalt complexes are rare.[33,34] Without STM image simulations, one might expect the Co atom to sit at the brighter side of the complex. However, in accordance with observations for higher Co coverage (see below), we suggest that the Co atom causes the depression and attribute the counterintuitive STM contrast to a modified molecular conformation, where alkynes next to Co spread apart, implying that non-interacting terminal groups are pushed upward (brighter appearance).

A closer look at the two protruding lobes of the C_1 units (Figure 2d) reveals that one lobe appears brighter than the other, thus the complexes exhibit chirality. We define a C_1 unit to represent the 'R' enantiomer for the case that the brighter protrusion is on the right side of the dashed line when going from the cobalt atom toward the brighter side. Interestingly, when analyzing the handedness of the C_1 units within the β domain depicted in Figure 2c, it turns out that all complexes exhibit the same handedness (Figure 2d). Consistently, within an α domain, only the opposite handedness was observed (see Figure S3c). Based on the observation of six orientations of C_1 within organic domains, we propose its adsorption on a six-fold symmetric adsorption site (top site) and superimposed a gas-phase DFT-calculated model, aligned according to the molecular orientation within β domains, on the Ag(111) registry (Figure 2d). The related situation for the α domain is depicted in Figure S3c. In both cases, six hollow sites are found very close to where the Co atom is expected from the gas-phase model (crossing of black dashed circle and dashed lines). Considering the tendency of Co atoms to adsorb at the hollow sites[35] along the periphery of the dashed circle (12 hollow sites), combined with a strong Co-bisalkyne π-tweezer binding motif (six binding sites for HEB), we can explain the six orientations of C_1 within the α domain and its six orientations within the β domain. Assuming that the minimal Co dosage at 12 K does not alter the epitaxy of the whole domain, this finding confirms our tentative model of the centers of HEB monomers adsorbing on top sites within the organic phase. The chiral configuration of the organocobalt complexes supposedly results from the interplay of the epitaxy with the underlying Ag(111) surface and the intermolecular interactions with the organic template. With the objective to establish two Co-bisalkyne motifs within one HEB unit (*i.e.*, a dicobalt complex), the Co dosage at 12 K was increased. However, instead of well-defined dicobalt complexes, we observe irregular Co clustering on the immobile molecular template. Consequently, the influence of the deposition temperature on the formation of organocobalt complexes was studied next.

Co Dosage at 200 K. To investigate the influence of thermal activation on the formation and positioning of the complexes, we increased the sample temperature during Co dosage to a value (200 K), at which predeposited molecules are mobile. We prepared two samples with different stochiometric ratios (Co/HEB). Figure 3a−c refers to the low Co coverage, while the data shown in Figure 3d−f were obtained for the high Co coverage. Already at a low Co-molecule ratio (Figure 3a), one can observe the emergence of a new phase with a similar hexagonal packing scheme, but with a different unit cell containing both complexes and pristine molecules. The two domain orientations of this multicomponent phase differ from the organic phase by an ∼30° rotation of the embedded units (highlighted by hexagonal contours). The previously introduced α (β) notation is consistently reused for the organocobalt phase based on the fact that rotation of the organic α (β) unit cell by 31.3° [sum of R 8.9° and R 22.4° from Wood's notation for organic and organometallic adsorption phase (see above and below)] leads to the organometallic α (β) domain orientation.

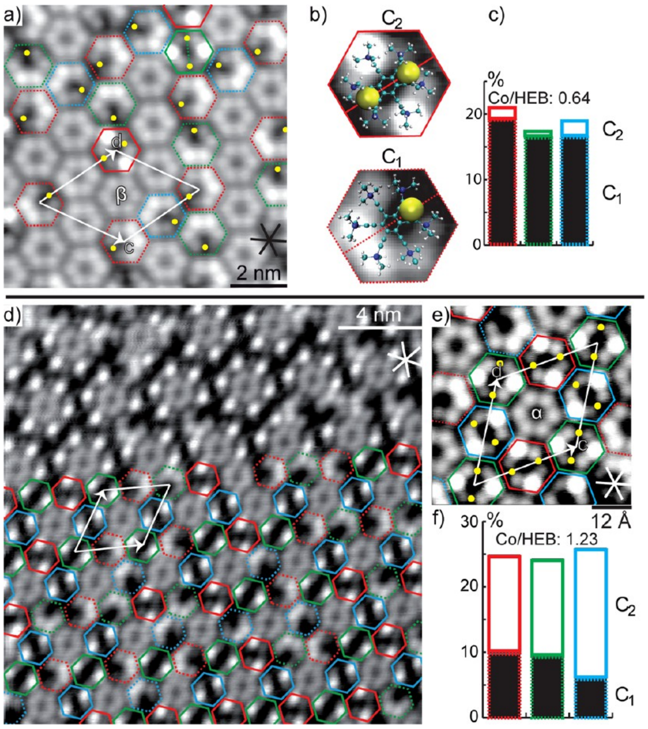

Figure 3. Organocobalt phase, generated *via* Co dosage at 200 K, displaying α domain (d, e) and β domain (a). The Ag(111) close-packed directions are shown by stars. (a) Organocobalt island with a Co-HEB ratio of 0.64 together with superimposed unit cell, cobalt markers (yellow), and colored outlines marking the main axes (MA). Complexes with the same MA (color) appear on positions coinciding with points of a hexagonal lattice. (b) Magnified STM image of two complex species with same MA within the network: mononuclear complex C_1 (dashed outline) and dinuclear complex C_2 (solid outline) incorporating one and two Co atoms along their MA (drawn line). (c) Relative occurrence of C_1 (dashed) and C_2 (solid) for each MA (ensemble of 267 units) for low-coverage case. (d) STM image of organocobalt network with Co-molecule ratio 1.23. (e) Pristine molecule surrounded by six C_2 resembling windmill blades. (f) Relative occurrence of C_2 and C_1 (171 molecules evaluated) for high-coverage case. Tunneling parameters V_t, I_t: (a, b) 100 mV, 300 pA; (d) 100 mV, 100 pA; (e) 20 mV, 100 pA.

In agreement with the *in situ* Co dosage at low temperature (*cf.* Figure 2c,d), the organometallic complexes appear in six orientations within one domain, which are classified by three 120° multiple main axes (MA); one of them shown for the C_1 orientation in Figure 3b (dashed line). For clarity, the MA of the complexes shown in Figure 3a,b,e are not depicted, but are inferred from the color scheme of their hexagonal contours. In addition to mononuclear C_1 (dashed outline), a less frequent species (solid outline) is recognized exhibiting two bright lobes opposite to each other and two depressions along the main axis (Figure 3b) rotated by 90° with respect to the protrusions. Consistently with C_1, which shows one depression, the second species is attributed to a dinuclear complex featuring two π-tweezer binding motifs along the MA. Hence, the intramolecular STM contrast is tentatively ascribed to a downward pulling of alkynes next to Co atoms, while non-interacting moieties are pushed upward for steric reasons and thus appear very brightly. We denote this species C_2 and highlight all Co atoms of the recognized complexes by yellow markers for better apprehension of the STM image. Figure 3b shows two magnified sections with superimposed DFT molecular models (gas-phase DFT model for C_1 and DFT model including surface for C_2), which represent two complexes with the same MA. With its Co atom having two possible adsorption sites along the MA, the C_1 complex can assume two orientations with the same MA.

An intriguing observation is that all complexes displaying the same MA orientation (same color) represent one subset of hexagonal lattice points. Since there are three MA, each alignment of Co-HEB, *i.e.*, a term referring to both the C_1 and C_2 species, is assigned to one of three hexagonal lattices shifted against each other. When filling both the remaining "free" spots of the three hexagonal lattices and remaining voids with pristine molecules, a dense-packed domain structure is established.

A representative large-scale STM topograph of the high-coverage sample with twice the Co-molecule ratio is presented in Figure 3d. Compared to the previous case, pristine molecules mainly occupy sites (representing one hexagonal lattice) where complexes are not expected due to their site-selective adsorption behavior. Consistently with the preceding results, complexes only occupy three hexagonal lattices according to their MA, thus establishing a periodic nanostructure divided into four hexagonal lattices: a hexagonal lattice of pristine molecules, appearing without protruding features, coexistent with three fault-free hexagonal lattices embedding mainly C_2 complexes (solid) and a few C_1 (dashed). A scenario where all six complexes surrounding one molecule are dinuclear is displayed in the close-up STM image of Figure 3e, whereby the positions of the Co atoms are given to guide the eye. The windmill-like motif is rationalized by three pairs of opposite complexes, where each pair reveals a different MA.

The relative occurrence of C_1 and C_2 within the molecular islands with low (high) Co coverage is displayed in the respective histogram in Figure 3f, representing an evaluation of 267 (173) molecules. The similar height of the three color-coded columns indicates that all three MA are equally probable

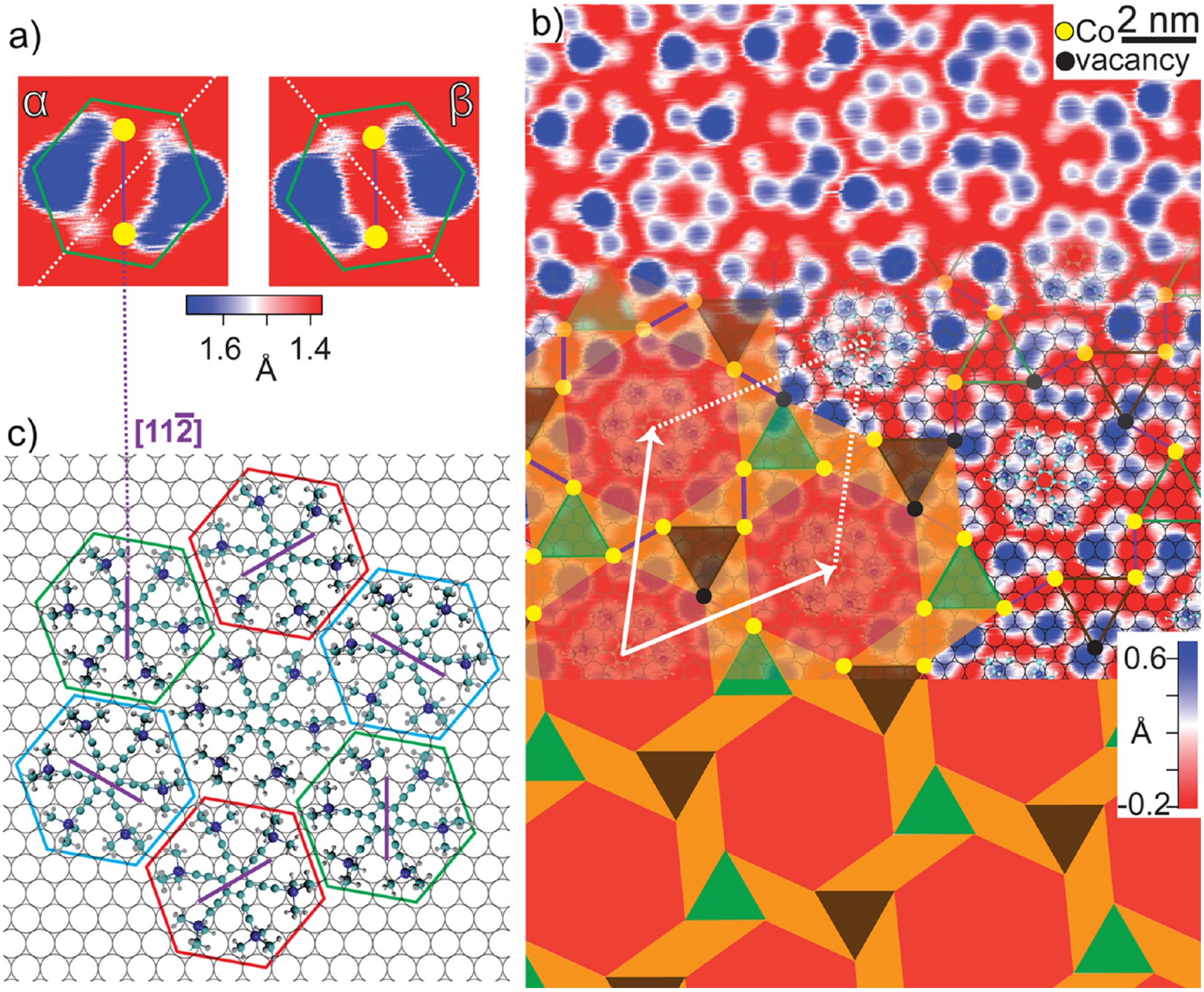

Figure 4. STM images with enhanced contrast displaying isolated C_2 conformers (α and β) and the organocobalt phase (α domain only). (a) Two STM images of isolated C_2 with same MA but opposite handedness. (b) High-resolution scrutinization of organocobalt domain with underlying Ag(111) lattice and superimposed molecular models. Co sites (yellow) and vacancies (black) of C_1 and C_2 coincide with fcc and hcp hollow sites. Co centers of complexes are connected by fcc and hcp triangles (color coded), which together with rhomboids (orange) and hexagons (red) span a chiral 3.4.6.4 surface tessellation pattern. (c) Adsorption model for windmill-motif (*cf.* Figure 3e) based on arranging molecules according to (b). Straight lines connecting opposite hollow sites (purple) coincide with MA orientations in (b) (purple-colored Co−Co axis). Tunneling parameters V_t, I_t: (a) −10 mV, 30 pA; (b) −10 mV, 100 pA.

for C_1 (black fill with dashed outline) and C_2 (white fill with solid outline). In the case of low Co dosage, 40% of the molecules remain pristine, while the complexes primarily represent the C_1 species (dashed outline). At high Co dosage, however, only 26% are not complexed, while C_2 is the more abundant complex species (solid outline). The strong decrease of the C_1 species further hints to the incorporation of two Co atoms within the C_2 species.

As a result of this analysis, the ordering of complexes is independent of the Co coverage, *i.e.*, Co-HEB always occupies three of four hexagonal lattices of the domains, while HEB substituting the lack of Co-HEB does not show any preferential adsorption site. Hence, a rhombic region of four adjacent molecules within an organocobalt domain can contain $0 \leq n \leq 6$ Co atoms.This implies that the strict ordering pattern is mainly ascribed to the adsorption behavior of the organocobalt complex. When increasing the Co/HEB ratio beyond 1.5, *i.e.*, the value of the ideal architecture (all complexes are dinuclear), we observed the complete dissolution of the mixed domains leaving behind scattered units, *i.e.*, isolated C_2 complexes and cluster-like structures containing Co and HEB in a highly irregular fashion (see Figure S4b). From the absence of open-porous domains of complexes, we conclude that to induce and stabilize the formation of 2D organocobalt domains, at least one-fourth of all constituents must remain pristine HEB.

While deposition at 12 K leads to statistically distributed C_1 orientations due to Co adsorption on an immobile molecular template, C_1 units formed at 200 K show a strong correlation between orientation and adsorption site due to the mobility of HEB and Co-HEB. From the observation that molecular deposition at 200 K leads to extended assemblies, we assume that the organocobalt phase requires the mobility of the on-surface formed complexes. Against the scenario that Co adatoms hop between molecular hosts speaks the ~30°

rotation of each unit within the new phase, compared to molecules of the pristine phase. Due to the strong distance dependency of electrostatic interactions, we exclude their influence on the highly selective positioning and alignments of Co-HEB. Combining the preferential adsorption of single Co adatoms at hollow sites together with the complexes' size and symmetry, and the selective bonding of Co atoms *via* alkyne−Co−alkyne bridges, the organization of the organocobalt domains is explained by the adsorption site-selective positioning of Co-HEB units on Ag(111).

Surface Tessellation. For a better understanding and atom-precise characterization of the intricate layer organization, we present high-resolution STM images with enhanced contrast for both isolated C_2 units (Figure 4a) and extended domains (Figure 4b). Isolated C_2 complexes coexist as a naturally formed species with 2D networks (see Figure S4). Due to the enhanced contrast for the complex depicted in Figure 4a, an uneven apparent height of the two lobes near to each Co position (yellow marker) is noticeable, whereby the two less protruding features are connected by a white line for simple identification. This α configuration is compared to a β C_2 unit, which reflects the same MA (purple line), however, it appears slightly rotated and the intramolecular contrast of the alkynes next to Co appears inverted (mirrored white line). From the different angles between the MA and the depicted lines, we identify the chiral character of the dinuclear organocobalt complexes, labeled α and β according to their mirror-symmetry with respect to the MA. The chiral signature could be interpreted as slightly different z-heights within each alkyne pair enclosing a Co atom, and it seems remarkable that both bisalkyne Co motifs of one complex display the same handedness. The existence of enantiomeric forms of the C_2 complex demonstrates that chirality is present at the single-complex level and is not induced by the aggregation into a 2D domain only.

To establish a direct atomic-level comparison with the 2D organocobalt phase, an STM image with similar enhanced contrast is presented in Figure 4b together with the underlying Ag(111) lattice. First, a different apparent height of alkynes interacting with Co is identified for both C_1 and C_2, and second, their bisalkyne Co motifs reflect the same chirality. Therefore, we conclude that this image shows an enantiopure domain in which the C_2 complexes correspond to the α conformer of Figure 4a. As expected, analyzing the enhanced STM contrast of an organometallic β domain reveals homochiral entities coinciding with single β conformers (see Figure S5). Both isolated and laterally embedded α (β) conformers exhibit the same molecular alignment with respect to their underlying $[11\bar{2}]$ directions, representing their mirror-symmetric axes. There is approximately a 16° twist between α and β conformers. Compared to a racemic arrangement of these units,[36,37] the organization within domains of homochiral complexes is assumed to promote a closer domain packing, which implies stronger van der Waals interactions and hence a gain in adsorption and free energy.

A closer look at the proposed model for the α domain (Figure 4b) reveals that molecules and complexes are aligned in such a highly ordered fashion and that all Co positions fall onto substrate hollow sites. The missing Co atoms with respect to the ideal structure (*cf.* Figure 3e) are marked as black circles. The two Co atoms belonging to one C_2 complex always occupy one fcc and one hcp hollow site. They are connected by purple lines in order to highlight the complex's MA. Interestingly, the Co atom of C_1 is also located at either fcc or hcp hollow site, indicating that the presence of C_1 does not disturb the highly organized superlattice of incorporated Co atoms.

When linking the fcc (hcp) hollow sites of three adjacent complexes by an fcc (hcp) triangle and further connecting an fcc and hcp triangle by a rhomboid, a 3.4.6.4 tiling pattern[38] is clearly evident (lower part of Figure 4b). As highlighted by the colored polygons, one large hexagonal tile is surrounded by six triangles, three oriented upward (green) and three oriented downward (brown), and six rhomboids (orange). The unit cell contains one hexagon, two antiparallel triangles, and three 120° multiple rhomboids. The corners of the polygons are situated at hollow sites where Co is located. For the sake of completeness, we present the other handedness for the β domain (see Figure S5) and mention that both domains are mirror-symmetric with respect to the three MA (purple lines). As a note, we mention that the two-fold degenerate alignment of C_1 is attributed to the Co atom sitting at either fcc or hcp hollow site, however both configurations are not found with equal probability (see Figure S6).

The mathematical description of this structure dates back to Johannes Kepler, who deduced that the complete filling of an Euclidean plane with symmetric polygons can lead to just 11 tessellation structures.[39] Hitherto, numerous examples of surface tessellation have been reported, *e.g.*, a Kagomé lattice using dicarbonitrile linkers,[40] snub-square tiling within a lanthanide-based metal−organic framework,[41] and a rhombitrihexagonal tiling in a solution-confined oligophenylene-ethylene-based Pd(II) complex;[42] the latter motif is equivalent with our surface-confined tessellation pattern.

From a detailed analysis of both domains, we deduce a commensurate $\sqrt{129} \times \sqrt{129}$ R 22.4° superstructure with the α unit cell reading:

$$\begin{pmatrix} \vec{c} \\ \vec{d} \end{pmatrix} = \begin{pmatrix} 8 & 5 \\ -5 & 13 \end{pmatrix} \begin{pmatrix} \vec{u} \\ \vec{v} \end{pmatrix}$$

in matrix notation, where $\vec{u}$ and $\vec{v}$ are the primitive vectors of Ag(111), which were depicted in Figure 2b. The β unit cell reads in matrix notation: $\begin{pmatrix} 13 & -5 \\ 5 & 8 \end{pmatrix}$, as shown in Figure 3a and in the right part of Figure S5b. Consistent with our analysis of the organic phase, we encounter the pristine molecules' centers adsorbed at top sites, while the center of the complexes reside at bridge sites. The latter agrees with our symmetry consideration that both the STM appearance of Co-HEB and underlying bridge site share the same 120° multiple orientation and two-fold symmetric axis (MA).

To rationalize the emergence of the apparent windmill-like tiling motifs, *i.e.*, a pristine molecule surrounded by six complexes (*cf.* Figure 3e), Figure 4c displays the Ag(111) lattice with superimposed molecules, which are positioned and oriented corresponding to the α domain's registry in Figure 4b. Since we encounter a pair of hollow sites, one fcc and one hcp site, in close proximity to the Co positions of the gas-phase configuration of the complex (purple line), we suspect that the MA of complexes is determined by the favorable Co epitaxy and aligns accordingly, *i.e.*, perpendicular to the connection of the two substrate atoms forming the bridge site. Assuming that the orientation of the complex is correlated with its adsorption site, the intriguing surface tessellation pattern can be explained. In the case of a dense-packed molecular matrix and sufficient

Co atoms, three-fourths of the molecules can form two-fold symmetric complexes, which will be centered at bridge sites. The remaining one-fourth of molecules is necessary to complete the remaining voids with the six-fold symmetric precursors' centers located on top sites, which would be unfavorable for the complexes. As a note, the significant asymmetry of the π-tweezer Co bonding following from this simplified model (Figure 4c) may imply intramolecular relaxation due to flexible bending of interacting alkynes and slight displacements of Co with respect to the deeper lying hollow sites. Regarding the ability of isolated C_2 to express enantiomeric states (*cf.* Figure 4a) and 120° multiple orientations (colored outlines in Figure S4), we conclude based on comparison with Figure 4b that the isolated and incorporated complex exhibits the same adsorption behavior. An adsorption model for a single C_2 unit is shown in Figure S8d (left column).

DFT Results for the Organocobalt Phase. For a characterization of the extended supramolecular tessellation from a theoretical point of view, state-of-the-art DFT calculations including the Ag(111) substrate were performed. The input of this DFT calculation is based on positioning Co adatoms on a molecular lattice according to the experimentally observed organocobalt phase. To check reproducibility, the calculations were carried out with two different approximations of the exchange and correlation term (see Methods section). Both the revPBE+D3 and B86r-vdW-DF2 treatment provide very similar results, therefore only the results with the former procedure are presented.

A visualization of the lowest-energy geometry of the organocobalt phase is presented in Figure 5. To facilitate comparison with the experimentally observed structure (Figures 4a,b and Figure S5a,b), the Ag atoms in Figure 5b,c are represented by red (instead of gray) spheres. Notably, the DFT calculations corroborate the on-surface formation of dinuclear compounds with a Co−Co distance of 7.76 Å (Figure 5b). It is worth mentioning that this distance is close to twice the Co−arene distance (3.96 Å) of the gas-phase DFT model of C_1 (*cf.* Figure 2d), which suggests a minor influence of the Ag(111) surface on the Co−arene distance during $C_1 \rightarrow C_2$ conversion.

The DFT structure of the organocobalt domain has a unit cell with six Co atoms (yellow) and four molecules (white outline in Figure 5c), which agrees well with the observed α domain (*cf.* Figure 4b). Consistent with experiment, molecules without Co atoms are centered on top adsorption sites, while complexes are centered at bridge sites, thus establishing the observed windmill-like motifs (*cf.* Figures 3e and 4c). With the Co atoms preferentially binding close to fcc (hcp) hollow sites and representing the corners of superimposed brown (green) triangles, the experimentally observed tessellation pattern is fully reproduced.

To elucidate the arrangement of substrate atoms below the organocobalt phase, Figure 5a shows the topmost Ag atoms of a five-layer Ag(111) slab with a color coding and scaling according to labeled z-height intervals, whereby $z = 0$ defines the topmost layer. The Ag atoms with the lowest (highest) z values are exclusively encountered below the complexes, *i.e.*, two red (blue) Ag atoms along the Co−Co axis (perpendicular to it). The Ag atom below each alkyne-Co-alkyne motif is indented (red), while the Ag atom below each non-interacting TMS-alkyne moiety of C_2 is protruding (blue). Since the surface corrugation of the topmost Ag(111) layer is absent below the HEB molecules, we assume that it originates from the embedded Co atoms of the complexes. We consider that the complexes are pulled down *via* Co atoms, by which a strong interaction between alkynes and Ag atoms is only present for complexed HEB. For each complex, the d orbitals of each of the two protruding Ag atoms (blue) might strongly hybridize with the out-of-plane π orbitals of the overlying alkyne. The remaining four alkynes' in-plane π orbitals are supposed to strongly hybridize with the d orbitals of Co instead, wherefore the Ag atom below each alkyne-Co-alkyne motif (red) is lowered. The periodicity and distribution of the surface

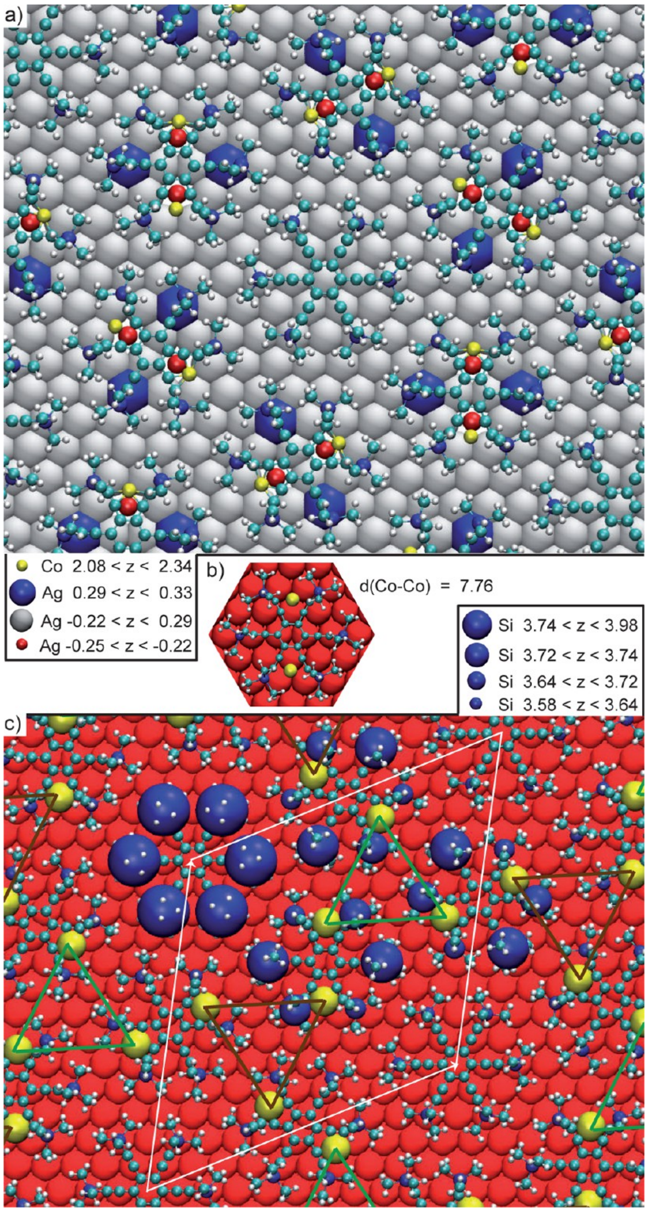

Figure 5. DFT modeling of surface-supported C_2 and pristine molecules within the α domain. (a) DFT representation emphasizing the corrugation of the topmost Ag(111) layer, as indicated by z-height intervals and scaled spheres representing indented (red) and protruding (blue) Ag atoms. Diameter of Co atoms is reduced in (a) and (b) for better visibility of substrate atoms. (b) Top view of single surface-supported C_2. (c) DFT model highlighting the varying z-height of the Si atoms by scaled spheres (blue) within the unit cell (white outline). The superlattice of embedded Co atoms is grouped by fcc and hcp triangles. Numeric values are in Å.

DOI: 10.1021/acsnano.6b06114
ACS Nano 2017, 11, 1347−1359

corrugation (0.58 Å height difference between blue and red spheres) agrees with the STM contrast observed in Figure 3e, where the complexes' non-interacting moieties show the strongest brightness, while the darkest contrast is found at the Co sites.

From the increased surface-molecule interaction of Co-HEB, we expect its lowering compared to HEB. Indeed, when comparing the physical heights of all carbon atoms (SI Figure S7b), the interacting C(sp) atoms of Co-HEB are lowered by 0.65 Å compared to the C(sp) atoms of HEB. As a consequence of this alkyne-Co-alkyne anchoring at hollow sites, the arene ring (C(sp^2) atoms) of Co-HEB is lowered by 0.26 Å. These molecular conformations brought about by the incorporation of Co atoms are caused by a strong bending of the alkynes next to Co (see Figure S7a).

Comparing the heights of the Si atoms, as illustrated by the scaled diameters of prominent blue spheres within the unit cell of Figure 5c, one notices the equal *z*-height of the six Si atoms of pristine HEB. On the contrary, for C$_2$, the two Si atoms of the TMS-alkyne-Co-alkyne-TMS binding motifs systematically display different heights, which implies a non-uniform alkyne-Co-alkyne interaction and is visible by strong bending deformations of the respective moieties. Consequently, the DFT calculation confirms the formation of an enantiopure organocobalt domain and rationalizes the chiral character of C$_2$ by the bending of the two alkynes next to Co. Although the physical heights of the simulation image cannot be directly related to the STM image contrast of Figure 4b, it should be mentioned that the TMS-alkyne being closer to Co appears brighter in the STM contrast, while the DFT image represents it with a smaller Si height than the less interacting moiety of the alkyne-Co-alkyne motif. The fact that the TMS groups of HEB appear less bright than the non-interacting TMS groups of Co-HEB is not reflected within the DFT visualization of the Si and C heights (Figures 5c and S7b), but is explained by the corrugation of topmost Ag atoms below the complexes (see above). Since the STM contrast reflects a convolution of both the *z*-height and electronic density of states, this discrepancy can be related to electronic effects contributing to the STM appearance.

A difference between the DFT structure and the model derived above from our STM observations is that the molecules are slightly rotated with respect to the experimental α domain configuration. This might be due to a limited accuracy of the DFT results in reproducing the delicate balance between Ag-alkyne and alkyne-Co-alkyne interactions.

Single-Molecule Manipulations on C$_2$. To inspect the structural integrity and conformational flexibility of isolated complexes, we performed single-molecule manipulation experiments. The STM image in Figure 6a shows isolated C$_2$ units together with small close-packed islands. Interestingly, at both low and high Co concentrations, single C$_2$ entitites coexist with assembled structures (see Figure S4a,b). The histogram in the inset is based on counting isolated C$_2$ species according to their MA. It reveals that all three orientations coexist with nearly equal probability within the evaluated region of 200 × 200 nm^2.

Figure 6b depicts STM images before and after a 120° rotation induced by the STM tip. For this purpose, we centered the tip on C$_2$, opened the feedback loop, and approached the tip from the set point (V_t = −10 mV, I = 50 pA) until current spikes indicated a rotation of C$_2$, in response to the increased tunneling current (typically at I = 20 nA). The similarity of the molecular features before and after the rotation implies the preservation of the chemical structure of C$_2$ upon this kind of manipulation, thus demonstrating the robustness of the C$_2$ complex.

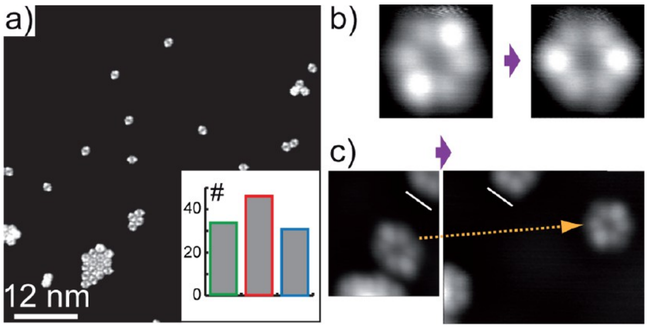

Figure 6. STM-tip manipulations on isolated C$_2$ complexes. (a) STM image illustrating isolated C$_2$ units distributed over a Ag(111) terrace. Inset: Histogram of MA orientations. (b) STM images after tip manipulation showing a 120°-rotated species. (c) Sequence showing a tip-assisted displacement of C$_2$ (along the depicted line) and associated rotation by 120°. Tunneling parameters for imaging V_t, I_t: (a−c) −10 mV, 50 pA.

The complexes' stability toward high tunneling currents, as long as the bias voltage remains low, was further used to demonstrate their cohesion and intactness toward lateral displacements. Figure 6c presents STM images of the complex before and after the lateral movement along the marked line. This displacement was achieved by approaching the tip until reaching I_t = 25 nA and dragging the complex along the path of the tip with respect to a fixed reference mark (white line). While attemps in manipulating pristine molecules resulted in molecular adsorption on the tip, isolated complexes could easily be moved without triggering any structural modification, as evident from the consecutive STM images. The latter implies a stronger interfacial coupling for Co-HEB compared to HEB. The 120° rotation of the complex after the manipulation hints to a correlation between its MA and adsorption site. Also the 120° rotation of a C$_2$ unit embedded in an organocobalt domain was achieved (see Figure S8). In this case, a significant increase in the measured height of the entire complex is evident. We tentatively assign it to a geometric lifting and rationalize it by an unfavorable adsorption site for this complex. Therefore, when, after rotation of the complex, its migration to a nearby hollow site with favorable $[11\bar{2}]$ orientation is sterically hindered by the surrounding molecules, the complex is stuck in an unfavorable configuration where Co atoms cannot reach the preferred hollow sites, presumably lifting the whole unit.

Kondo Signature of Activated Complexes. Complexes incorporating multiple magnetic metal centers[9,43,44] are discussed as promising candidates for nanomagnets, spintronic, and quantum computing devices.[45−47] The focus lies particularly on surface-supported molecular magnets expressing long magnetic lifetimes[48−50] and remarkable hysteresis characteristics.[51] Accordingly, we explored the properties of isolated complexes regarding potential magnetic behavior. Initially, we performed scanning tunneling spectroscopy (STS) measurements on isolated C$_2$ units, which do not show a Kondo feature. Then, we applied a stronger manipulation procedure than before, in order to alter the interaction between Co atoms and alkynes: the STM images I and II of Figure 7a were obtained after applying a bias pulse of −2 V for a duration of 10 ms on top of the left bright lobe

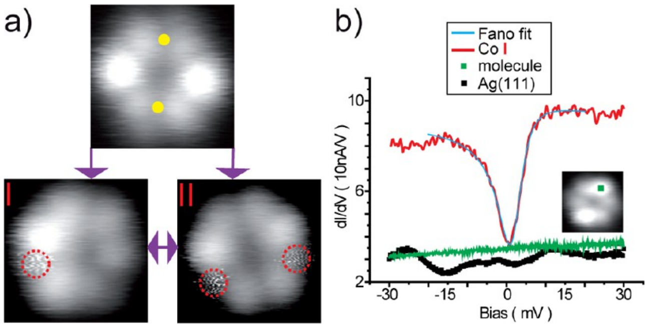

Figure 7. Kondo features in activated C_2 species. (a) Activation of pristine complex (upper panel) by a bias pulse (−2 V, 10 ms) with the tip positioned above a bright lobe. Occurrence of one (two) frizzled spot(s) (red outline) in activated species I and II, along with a reduced brightness of one (two) protrusion(s), and a rotation of HEB. (b) Low-bias dI/dV spectra on pristine Ag(111) (black) and C_2 [green: spectrum on pristine complex acquired at position of green marker in the inset in (b), and red: spectrum acquired within red circle of configuration I in (a)]. The Fano fit (blue) was carried out with $q = 0.27$, $x_0 = 1.9$ mV, $T_K = 23$ K. Tunneling parameters for imaging V_t, I_t: (a, b) STM and STS set point: −20 mV, 100 pA. STS set point parameters: −20 mV, 100 pA (120 pA for Kondo spectrum), $\Delta z = -90$ pm before sweep, $V_{mod} = 1$ mV rms, $f = 933.5$ Hz, $T = 1.2$ K.

(upper image). The structurally modified complex I is characterized by a slight rotation, one remaining protrusion, and a grainy frizzled feature (red outline) located between two alkynes. The manipulation experiments were repeated for different complexes and show that configuration I is highly reproducible. Occasionally, a voltage pulse on a protrusion triggered the emergence of a strongly rotated compound with two grainy frizzled features, as identified by two outlined spots in configuration II. A further voltage pulse on configuration II converted it back to I, identifying the latter as more stable.

Interestingly, the frizzled features of the I and II variants in Figure 7a appear at different locations compared to the Co sites of the initial structure above. We attribute them to loosely bound Co atoms losing their initial binding sites and changing to a metastable binding configuration, in which they partially follow the STM tip. In configuration I, one of the two Co atoms has undergone this site change, while in configuration II, both Co atoms have changed their adsorption sites. While the transformation from I to II is reversible, we could not convert the activated complex to pristine C_2.

When performing dI/dV spectroscopy above a frizzled feature of the activated configuration I (red outline, Figure 7a), we observed a strong Kondo resonance. The low-bias STS spectrum exhibiting a dip-like structure is shown in Figure 7b together with dI/dV spectra on pristine Ag(111) and C_2, both revealing a featureless shape (STS data obtained at 1.2 K). We suggest that the dip feature indicates the existence of a magnetic moment that is screened by the surrounding electrons, giving rise to a many body state.[52] The shape of the Kondo resonance shown in Figure 7b has been reproduced on many activated C_2 species (configuration I) with different STM tips. It was fitted by the Fano equation:

$$dI/dV \propto \frac{(q\Gamma + E - E_0)^2}{\Gamma^2 + (E - E_0)^2}$$

where E_0 and Γ are the position and temperature-dependent half width at half-maximum of the Kondo feature and q is the shape parameter giving different weight to the interfering quantum-tunneling paths. After eliminating thermal broadening and modulation voltage (root-mean-square values V_{rms}) broadening by the formula:

$$\Gamma(T) = \sqrt{(3.5k_BT)^2 + (\sqrt{6}\,eV_{rms})^2 + 2(k_BT_K)^2} \tag{1}$$

with k_B and e being respectively the Boltzmann constant and the elementary charge,[53,54] the obtained Kondo temperature reads $T_K = 23$ K. This value is remarkably lower than for isolated Co atoms on the Ag(111) surface (95 K).[55] The diminished value could be related to Co-alkyne orbital interactions weakening the Co-surface bond and thus the Kondo screening, which originates from the delocalized cloud of surface electrons. Configuration II (two grainy spots), which was rarely observed, also expressed a Kondo signature on both sides, but with different Kondo temperatures. Embedded C_2 entities within organocobalt domains can also be similarly activated to display a Kondo signature above the frizzled feature of configuration I. The observed Kondo resonance on STM tip-manipulated C_2 complexes reveals a chemical fingerprint of incorporated Co atoms, which further consolidates our interpretation of an on-surface formed dinuclear organocobalt complex.

Conformer Switching. The creation of single-molecule switches and molecular motors, which are powered by the tunneling electrons of a STM tip[56−59] or the STM tip's electrical field,[60,61] bears promising potential for nanoelectronic devices. Furthermore, STM represents an exquisite tool to identify switching between enantiomeric states of surface-adsorbed chiral molecules, *e.g.*, the vibration-induced switching of propene.[62]

Intrigued by the existence of the different conformer states (α and β) of the C_2 complexes, we explored the possibility to switch between C_2 enantiomers with the aid of the STM tip. The STM image in Figure 8a displays two isolated C_2 units, which, according to the brightness of the four alkynes next to Co, are recognized as β and α conformers (compare with Figure 4a). When imaging the α complex with an elevated tunneling bias ($V_t = 100$ mV), we observe a fuzzy appearance of isolated C_2 (right panel of Figure 8a). In subsequent imaging with low bias voltage (~20 mV), the same complex again appears stable and with a clearly discernible enantiomeric state. Accordingly, we attribute the fuzziness of the high-bias image to tip-induced switching between the α and β conformers. It seems to occur within a significantly smaller time scale compared to the acquisition time of the STM image.

To determine the critical bias voltage of this drastic transition in the appearance behavior, we recorded dI/dV spectra. They are displayed in Figure 8b and show two regimes separated by a threshold of ±40 mV. For bias voltages below the threshold, a stable signal with either low or high conductance is present, whereas beyond the threshold, a fluctuating signal is observed. The latter is assigned to repeated switching between the two enantiomeric states causing low and high conductance at the same tip position (*cf.* Figure 8c).

For better characterizing the switching behavior, we recorded a series of spectra over all of the TMS-alkyne groups involved in organometallic bonding (markers in Figure 8c), which are referred to as TMS 1, 2, 3, 4 in Figure 8c−f. At these four locations, we recorded time traces of the tip height changes with a closed feedback-loop, such as the example shown in Figure 8d. For each of these traces, we assign the abrupt

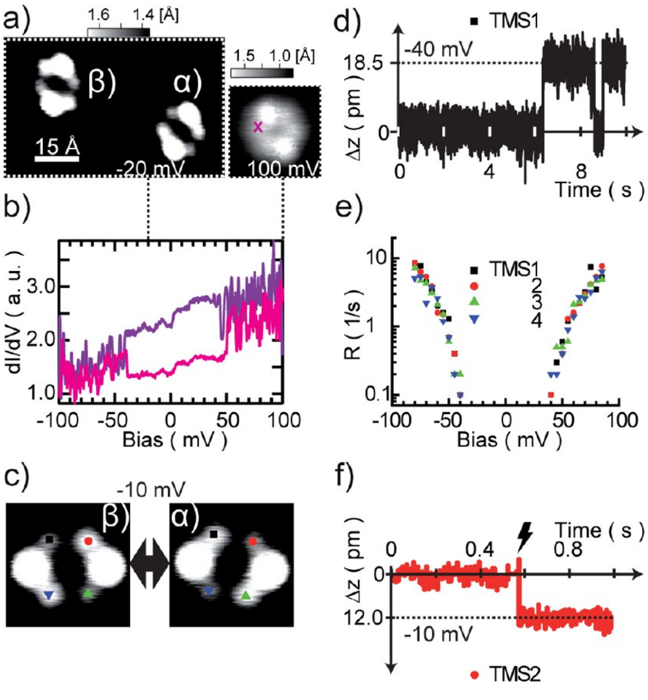

Figure 8. STM and STS results qualifying isolated C_2 as a chiral complex. Dashed vertical lines indicate the voltage at which STM images and time sequences were recorded. (a) STM topograph at −20 mV allows the differentiation of the α and β conformer, while the adjacent STM image at 100 mV appears frizzled. (b) Two subsequent dI/dV spectra obtained at spots marked in a) exhibit a symmetric threshold at ±40 mV and two-state fluctuations above it. (c) Enhanced contrast STM images before and after switching the chiral state, where marked molecular lobes flipped their brightness contrast. (d) $\Delta z(t)$ spectrum on top of a marked lobe for a bias voltage above threshold. Abrupt changes between plateaus indicate switching events. (e) Logarithmic plot of switching rate as a function of the bias voltage for TMS 1, 2, 3, 4 (markers). (f) Controlled switching by applying a short bias pulse while monitoring z-height below the threshold voltage. Tunneling parameters for imaging V_t, I_t: (a) −20 mV, 100 pA; inset: 100 mV, 300 pA; (c) −10 mV, 300 pA. STS set point parameters: (b) 100 mV, 300 pA, V_{mod} = 1 mV rms, f = 733.5 Hz, T = 4.5 K. Time sequences at T = 1.2 K: (d) −40 mV, 30 pA; (e) 30 pA; (f) −10 mV, 50 pA.

changes between plateaus of different z-height (offset Δz) to switching events between enantiomeric states and determine the switching rate by dividing the number of events by the acquisition time (10 s). The dependence of the switching rate on the bias voltage is shown for each of the four TMS-alkyne groups (markers) and at a constant tunneling current of 40 pA (Figure 8e). For all moieties, the logarithmic scale implies that an exponential trend is present for bias voltages above a threshold of about ±40 mV. The absence of the switching below the threshold value for both polarities is consistent with the behavior apparent in the STS spectra of Figure 8b. Hence, the switching is associated with an electron-driven process exciting molecular vibrations. To determine whether an event is triggered by only one electron,[58] the dependence of the switching rate on the tunneling current was studied. From the associated double-logarithmic representation together with a linear fit revealing a slope being slightly higher than unity (see Figure S9), we cannot exclude that the switching is caused by a higher-order electron process.

To control the switching process without triggering multiple switching events, a short bias voltage pulse (−75 mV and 45 ms) was employed while acquiring $z(t)$. As shown in Figure 8f, the apparent edge due to the pulse coincides with a jump in z, indicating a controlled single switching event. Recording STM images before and after such switching demonstrates that a single switching event suffices to reproducibly alter between the two enantiomeric states of a C_2 unit. Within the interacting TMS-alkyne moieties (marked molecular lobes in Figure 8c), diagonally opposite lobes appear with the same brightness, while adjacent lobes reveal an apparent height difference. Hence, we assume that the out-of-plane bending (oscillation) of these intramolecular lobes is coupled. For each switching process, all four interacting groups change z-height, whereby two diagonally opposite lobes oscillate in phase, while two adjacent moieties express opposite conformation states during this synchronous two-state switching.

In contrast to isolated C_2, it was not possible to switch the chirality of C_2 units embedded in the 2D organocobalt phase. According to our interpretation, a switching process represents an interconversion of the complex's handedness, which is accompanied by a rotation of the molecule (Figure 8c). Presumably, this process is prohibited due to steric interactions with the surrounding molecules in the densely packed chiral architecture, which represents a conglomerate phase. The switching of isolated Co-HEB shows the relationship between its two chiral states and the respective unit cell orientation of assembled domains. Both the isolated compound as well as the unit cell of the organic and organocobalt conglomerate phase reveal a twist of ~16° between α and β. During $\alpha \leftrightarrow \beta$ switching, the Co atoms along the MA of the isolated C_2 may remain at fixed locations or rotate (together with their molecular host) symmetrically to the complex's underlying bridge site. The latter scenario would be more consistent with the observed 120° multiple rotations of the Co−Co axis (MA) (*cf.* Figure 6b,c).

CONCLUSIONS

In summary, we have presented a systematic STM and DFT study of an on-surface synthesized dinuclear organocobalt complex, which was accomplished by the well-defined incorporation of Co atoms into a multitopic alkyne derivative on a smooth metal surface. The organometallic building blocks self-assemble into a 2D nanoarchitecture, whose incorporated Co atoms express a 3.4.6.4 surface tessellation. Atom-precise STM imaging and extensive DFT calculations unraveled the decisive role of the surface registry on the formation of the chiral tiling pattern. Tip manipulation experiments on isolated complexes demonstrated their conformational flexibility enabling reversible two-state switching between enantiomers and deepened our understanding of the structural properties of the 2D phase. A Kondo feature at modified complexes provided a chemical fingerprint for the incorporated Co atoms.

Our results open up new ways to generate nanoobjects with multiple spin-centers embedded within custom-designed molecular backbones, which is specifically interesting taking into account the extraordinary capabilities of the alkyne moiety to develop conjugated electronic states, as already demonstrated within a plethora of structures.[21,63−65] The STM tip-activated configuration of such complexes could represent an alternative approach toward nanomagnetism where wide tunability of the magnetic behavior is expected. Combining multinuclear alkynyl complexes with on-surface coupling reactions[66−68] could afford extended spin systems with a prospect for quantum information manipulation at the single-molecule level. Our results bear fruitful perspectives for interfacial organometallic chemistry and provide useful prospectives toward the atom-precise fabrication of functional interfacial nanoarchitectures with transition metal centers in well-defined environments.

METHODS

All sample preparations and STM measurements were carried out in the UHV environment of the preparation and STM chamber of a commercial Joule−Thompson scanning tunneling microscope (www.specs.de) with a base pressure below 1×10^{-10} mbar. The Ag(111) sample was cleaned by repeated cycles of Ar+ sputtering (0.9 kV, 10 μA emission) for 25 min (min) and subsequent annealing at 760 K for 15 min. The powder of purified HEB molecules (synthesized by Zhi Chen, Ruben group at Karlsruhe Institute of Technology) was thoroughly degassed and evaporated at a crucible temperature of 430 K, which caused a strong darkening of the initially yellow powder. The organic phase was prepared by CVD on the clean Ag(111) sample kept at 300 or 450 K. Co was sublimated from a thoroughly degassed Co wire of 99.995% purity (Alfa Aesar), which was wound around a tungsten wire that was thermally heated by a current. For the *in situ* deposition, an evaporator was placed in front of the cryostat's evaporation gate, which was opened for a certain time with the sample always staying below 12 K. For deposition at 200 K, the sample was placed by a precooled manipulator in front of an additional evaporator installed in the preparation chamber. During Co deposition, the power supply provided a voltage and current of V_d = 1.7 V, I_d = 6.4 A (1.2 V, 8.1 A) for the *in situ* (*ex situ*) deposition. The STM topographs were mainly acquired at liquid helium temperature (∼4.5 K), and if not stated otherwise, the constant current mode was used. Spectroscopic and manipulation measurements were mainly conducted at 1.2 K with an etched tungsten tip that was sputtered, Ag-coated by field-emission and prepared by soft indentations on the smooth Ag(111) surface, until a clear signature of the surface state was present. For dI/dV spectroscopy, an external lock-in amplifier was used at a frequency of f = 733.5 and 933.5 Hz and modulation voltage of V_{mod} = 1 mV rms (low-bias spectra).

We performed the DFT calculations within the Kohn−Sham scheme. We used the TurboMole code in the gas-phase (isolated cluster) calculations and the QuickStep module[69] in the CP2K[70] package for the surface calculations. In the calculations with TurboMole, we employed the def2-TZVPP Gaussian basis set, expanded the electronic wave functions, and the Perdew−Burke−Ernzenhof (PBE)[71] generalized gradient approximation (GGA) as the approximation for the exchange−correlation functional. Furthermore, we included the D3 dispersion correction[72] in order to be more consistent with the calculations at the surface, even if, in the gas phase molecule, this is not relevant.

In the CP2K calculations, we employed two different approximations to the exchange−correlation term: a revised-PBE (revPBE)[73] GGA together with the D3 dispersion correction and a density functional that contains an explicit non-local term for the London dispersions. In the latter, we employ the vdW-DF2[74] form with the revised B86 gradient dependent or GGA part of the exchange functional. The wave functions in the Gaussian projector wave (GPW) method in QuickStep were expanded in the MOLOPT-DZVP basis set[75] and the density up to 700 Ry, with a value of 60 Ry for the REL_CUTOFF parameter. Only the Γ point was used to approximate the integral over the first Brillouin zone. 32 Å was the length of the cell along the surface normal, leaving more than 16 Å vacuum between the molecules and the opposite site of the slab. The occupation numbers were broadened using the Fermi−Dirac distribution, corresponding to an effective temperature of 500 K. We used the equilibrium lattice constant of 4.1074 Å obtained with the rB86-vdW-DF2 exchange−correlation functional in both cases. The geometry is very similar to the two treatments of the exchange and correlation effects (revPBE+D3 and B86r-vdW-DF2). Therefore, we only report one DFT treatment, *i.e.*, the revPBE+D3 results.

ASSOCIATED CONTENT

Ⓢ Supporting Information

The Supporting Information is available free of charge on the ACS Publications website at DOI: 10.1021/acsnano.6b06114.

> Synthetic details of HEB molecule. Preparation details on surface-adsorbed organic phase. Large-scale STM image on *in situ* Co dosage at 12 K, along with 'S' enantiomers (C_1) within α domain and related adsorption model. Large-scale STM images for optimal (excessive) Co concentration dosed at 200 K, resulting in extended organocobalt domains (phase dissolution). STM results showing surface tessellation for both organocobalt domains and derived adsorption models. Two-fold degenerate alignment of the C_1 species based on STM results evincing the coexistence of both domains within the same Ag(111) terrace. DFT-modeled visualization depicting physical heights of all carbon atoms within the organocobalt phase. Single-molecule rotation of C_2 within a molecular island and adsorption model for a single C_2 unit. Switching statistic for isolated C_2, *i.e.*, double-logarithmic presentation of switching rate versus current (PDF)

AUTHOR INFORMATION

Corresponding Author

*E-mail: florian.klappenberger@tum.de.

ORCID

Mario Ruben: 0000-0002-7718-7016
Ari Paavo Seitsonen: 0000-0003-4331-0650
Florian Klappenberger: 0000-0002-2877-6105

Notes

The authors declare no competing financial interest.

ACKNOWLEDGMENTS

With the support of the Technische Universität München, Institute for Advanced Study, funded by the German Excellence Initiative and the European Union Seventh Framework Programme under grant agreement no. 291763, the ERC Advanced Grant MolArt, and the China scholarship council (CSC). We also acknowledge the Karlsruhe Nano Micro Facility (KNMF, www.kit.edu/knmf) of the Forschungszentrum Karlsruhe for provision of access to the MALDI-TOF instrument at their laboratories. We gratefully acknowledge discussions with Yi-Qi Zhang.

REFERENCES

(1) Schreiber, F. Structure and Growth of Self-Assembling Monolayers. *Prog. Surf. Sci.* **2000**, *65*, 151−257.

(2) De Feyter, S.; De Schryver, F. C. Two-Dimensional Supramolecular Self-Assembly Probed by Scanning Tunneling Microscopy. *Chem. Soc. Rev.* **2003**, *32*, 139−150.

(3) Barth, J. V. Molecular Architectonic on Metal Surfaces. *Annu. Rev. Phys. Chem.* **2007**, *58*, 375−407.

(4) Kamat, P. V. Graphene-Based Nanoarchitectures. Anchoring Semiconductor and Metal Nanoparticles on a Two-Dimensional Carbon Support. *J. Phys. Chem. Lett.* **2010**, *1*, 520−527.

(5) Klappenberger, F. Two-dimensional Functional Molecular Nanoarchitectures - Complementary Investigations with Scanning Tunneling Microscopy and X-ray Spectroscopy. *Prog. Surf. Sci.* **2014**, *89*, 1−55.

(6) Auwärter, W.; Écija, D.; Klappenberger, F.; Barth, J. V. Porphyrins at Interfaces. *Nat. Chem.* **2015**, *7*, 105−120.

(7) Brune, H.; Gambardella, P. Magnetism of Individual Atoms Adsorbed on Surfaces. *Surf. Sci.* **2009**, *603*, 1812−1830.

(8) Enders, A.; Skomski, R.; Honolka, J. Magnetic Surface Nanostructures. *J. Phys.: Condens. Matter* **2010**, *22*, 433001.

(9) Bogani, L.; Wernsdorfer, W. Molecular Spintronics Using Single-Molecule Magnets. *Nat. Mater.* **2008**, *7*, 179−186.

(10) N'Diaye, A. T.; Bleikamp, S.; Feibelman, P. J.; Michely, T. Two-Dimensional Ir Cluster Lattice on a Graphene Moiré on Ir(111). *Phys. Rev. Lett.* **2006**, *97*, 215501.

(11) Brihuega, I.; Michaelis, C. H.; Zhang, J.; Bose, S.; Sessi, V.; Honolka, J.; Schneider, M. A.; Enders, A.; Kern, K. Electronic Decoupling and Templating of Co Nanocluster Arrays on the Boron Nitride Nanomesh. *Surf. Sci.* **2008**, *602*, L95−L99.

(12) Pan, Y.; Gao, M.; Huang, L.; Liu, F.; Gao, H.-J. Directed Self-Assembly of Monodispersed Platinum Nanoclusters on Graphene Moiré Template. *Appl. Phys. Lett.* **2009**, *95*, 093106.

(13) Natterer, F. D.; Patthey, F.; Brune, H. Ring State for Single Transition Metal Atoms on Boron Nitride on Rh(111). *Phys. Rev. Lett.* **2012**, *109*, 066101.

(14) Bazarnik, M.; Brede, J.; Decker, R.; Wiesendanger, R. Tailoring Molecular Self-Assembly of Magnetic Phthalocyanine Molecules on Fe- and Co-Intercalated Graphene. *ACS Nano* **2013**, *7*, 11341−11349.

(15) Schlickum, U.; Decker, R.; Klappenberger, F.; Zoppellaro, G.; Klyatskaya, S.; Ruben, M.; Silanes, I.; Arnau, A.; Kern, K.; Brune, H.; Barth, J. V. Metal-Organic Honeycomb Nanomeshes with Tunable Cavity Size. *Nano Lett.* **2007**, *7*, 3813−3817.

(16) Decker, R.; Schlickum, U.; Klappenberger, F.; Zoppellaro, G.; Klyatskaya, S.; Ruben, M.; Barth, J. V.; Brune, H. Using Metal-Organic Templates to Steer the Growth of Fe and Co Nanoclusters. *Appl. Phys. Lett.* **2008**, *93*, 243102.

(17) Pivetta, M.; Pacchioni, G. E.; Schlickum, U.; Barth, J. V.; Brune, H. Formation of Fe Cluster Superlattice in a Metal-Organic Quantum-Box Network. *Phys. Rev. Lett.* **2013**, *110*, 086102.

(18) Krenner, W.; Klappenberger, F.; Kühne, D.; Diller, K.; Qu, Z.-R.; Ruben, M.; Barth, J. V. Positioning of Single Co Atoms Steered by a Self-Assembled Organic Molecular Template. *J. Phys. Chem. Lett.* **2011**, *2*, 1639−1645.

(19) Long, N. J.; Williams, C. K. Metal Alkynyl Sigma Complexes: Synthesis and Materials. *Angew. Chem., Int. Ed.* **2003**, *42*, 2586−2617.

(20) Powell, C. E.; Humphrey, M. G. Nonlinear Optical Properties of Transition Metal Acetylides and Their Derivatives. *Coord. Chem. Rev.* **2004**, *248*, 725−756.

(21) Costuas, K.; Rigaut, S. Polynuclear Carbon-Rich Organometallic Complexes: Clarification of the Role of the Bridging Ligand in the Redox Properties. *Dalton Trans.* **2011**, *40*, 5643−5658.

(22) Wong, W. Y.; Ho, C. L. Organometallic Photovoltaics: A New and Versatile Approach for Harvesting Solar Energy Using Conjugated Polymetallaynes. *Acc. Chem. Res.* **2010**, *43*, 1246−1256.

(23) Whittell, G. R.; Hager, M. D.; Schubert, U. S.; Manners, I. Functional Soft Materials from Metallopolymers and Metallosupramolecular Polymers. *Nat. Mater.* **2011**, *10*, 176−188.

(24) Liu, J.; Chen, Q.; Xiao, L.; Shang, J.; Zhou, X.; Zhang, Y.; Wang, Y.; Shao, X.; Li, J.; Chen, W.; Xu, G. Q.; Tang, H.; Zhao, D.; Wu, K. Lattice-Directed Formation of Covalent and Organometallic Molecular Wires by Terminal Alkynes on Ag Surfaces. *ACS Nano* **2015**, *9*, 6305−6314.

(25) Guo, S.; Kandel, S. A. Scanning Tunneling Microscopy of Mixed Valence Dinuclear Organometallic Cations and Counterions on Au(111). *J. Phys. Chem. Lett.* **2010**, *1*, 420−424.

(26) Quardokus, R. C.; Lu, Y. H.; Wasio, N. A.; Lent, C. S.; Justaud, F.; Lapinte, C.; Kandel, S. A. Through-Bond Versus Through-Space Coupling in Mixed-Valence Molecules: Observation of Electron Localization at the Single-Molecule Scale. *J. Am. Chem. Soc.* **2012**, *134*, 1710−1714.

(27) Čechal, J.; Kley, C. S.; Kumagai, T.; Schramm, F.; Ruben, M.; Stepanow, S.; Kern, K. Functionalization of Open Two-Dimensional Metal-Organic Templates through the Selective Incorporation of Metal Atoms. *J. Phys. Chem. C* **2013**, *117*, 8871−8877.

(28) Weber, P. B.; Hellwig, R.; Paintner, T.; Lattelais, M.; Paszkiewicz, M.; Casado-Aguilar, P.; Deimel, P. S.; Guo, Y.; Zhang, Y.-Q.; Allegretti, F.; Papageorgiou, A. C.; Reichert, J.; Klyatskaya, S.; Ruben, M.; Barth, J. V.; Bocquet, M.-L.; Klappenberger, F. Surface-Guided Formation of an Organocobalt Complex. *Angew. Chem., Int. Ed.* **2016**, *55*, 5754−5759.

(29) Omae, I. Three Characteristic Reactions of Organocobalt Compounds in Organic Synthesis. *Appl. Organomet. Chem.* **2007**, *21*, 318−344.

(30) Lang, H.; Weinmann, M. Bis(alkynyl) Titanocenes as Organometallic Chelating Ligands for the Stabilization of Monomeric Organo Copper(I) Compounds. *Synlett* **1996**, *1996*, 1−10.

(31) Lang, H.; George, D. S. A.; Rheinwald, G. Bis(alkynyl) Transition Metal Complexes, $R^1C{\equiv}C$-[M]-$C{\equiv}CR^2$, as Organometallic Chelating Ligands; Formation of μ, $\eta^{1(2)}$-Alkynyl-Bridged Binuclear and Oligonuclear Complexes. *Coord. Chem. Rev.* **2000**, *206-207*, 101−197.

(32) Kovacs, A.; Frenking, G. Bonding Interactions of a Molecular Pair of Tweezers with Transition Metals. Theoretical Study of Bis(η^2-Alkyne) Complexes of Copper(I), Silver(I), and Gold(I). *Organometallics* **1999**, *18*, 887−894.

(33) Lang, H.; Herres, M.; Imhof, W. Stabiliziation of Low-Coordinated M(CO) Building-Blocks: Synthesis and Reactivity of $\{(\eta^5\text{-}C_5H_4SiMe_3)_2\ Hf(C{\equiv}CPh)_2\}$ M(CO) (M = Ni,Co). *J. Organomet. Chem.* **1994**, *465*, 283−287.

(34) Herres, M.; Lang, H. Stable (η^2-Alkyne)MCl_2 Complexes - Structure and Reactivity. *J. Organomet. Chem.* **1994**, *480*, 235−239.

(35) Kühne, D.; Klappenberger, F.; Decker, R.; Schlickum, U.; Brune, H.; Klyatskaya, S.; Ruben, M.; Barth, J. V. High-Quality 2D Metal-Organic Coordination Network Providing Giant Cavities within Mesoscale Domains. *J. Am. Chem. Soc.* **2009**, *131*, 3881−3883.

(36) Humblot, V.; Lorenzo, M. O.; Baddeley, C. J.; Haq, S.; Raval, R. Local and Global Chirality at Surfaces: Succinic Acid Versus Tartaric Acid on Cu (110). *J. Am. Chem. Soc.* **2004**, *126*, 6460−6469.

(37) Forster, M.; Dyer, M.; Persson, M.; Raval, R. 2D Random Organization of Racemic Amino Acid Monolayers Driven by Nanoscale Adsorption Footprints: Proline on Cu(110). *Angew. Chem., Int. Ed.* **2010**, *49*, 2344−2348.

(38) Chavey, D. Tilings by Regular Polygons II: A Catalog of Tilings. *Comput. Math. Appl.* **1989**, *17*, 147−165.

(39) Kepler, J. *Harmonices Mundi*; Johannes Planck: Linz, Austria, 1619.

(40) Schlickum, U.; Decker, R.; Klappenberger, F.; Zoppellaro, G.; Klyatskaya, S.; Auwärter, W.; Neppl, S.; Kern, K.; Brune, H.; Ruben, M.; Barth, J. V. Chiral Kagomé Lattice from Simple Ditopic Molecular Bricks. *J. Am. Chem. Soc.* **2008**, *130*, 11778−11782.

(41) Écija, D.; Urgel, J. I.; Papageorgiou, A. C.; Joshi, S.; Auwärter, W.; Seitsonen, A. P.; Klyatskaya, S.; Ruben, M.; Fischer, S.; Vijayaraghavan, S.; Reichert, J.; Barth, J. V. Five-Vertex Archimedean Surface Tessellation by Lanthanide-Directed Molecular Self-Assembly. *Proc. Natl. Acad. Sci. U. S. A.* **2013**, *110*, 6678−6681.

(42) Stepanenko, V.; Kandanelli, R.; Uemura, S.; Wurthner, F.; Fernandez, G. Concentration-Dependent Rhombitrihexagonal Tiling Patterns at the Liquid/Solid Interface. *Chem. Sci.* **2015**, *6*, 5853−5858.

(43) Zhang, L.; Bagrets, A.; Xenioti, D.; Korytár, R.; Schackert, M.; Miyamachi, T.; Schramm, F.; Fuhr, O.; Chandrasekar, R.; Alouani, M.; Ruben, M.; Wulfhekel, W.; Evers, F. Kondo Effect in Binuclear Metal-Organic Complexes with Weakly Interacting Spins. *Phys. Rev. B: Condens. Matter Mater. Phys.* **2015**, *91*, 195424.

(44) DiLullo, A.; Chang, S.-H.; Baadji, N.; Clark, K.; Klöckner, J.-P.; Prosenc, M.-H.; Sanvito, S.; Wiesendanger, R.; Hoffmann, G.; Hla, S.-W. Molecular Kondo Chain. *Nano Lett.* **2012**, *12*, 3174−3179.

(45) Luis, F.; Repollés, A.; Martínez-Pérez, M. J.; Aguilà, D.; Roubeau, O.; Zueco, D.; Alonso, P. J.; Evangelisti, M.; Camón, A.; Sesé, J.; Barrios, L. A.; Aromí, G. Molecular Prototypes for Spin-Based CNOT and SWAP Quantum Gates. *Phys. Rev. Lett.* **2011**, *107*, 117203.

(46) Aromi, G.; Aguilà, D.; Gamez, P.; Luis, F.; Roubeau, O. Design of Magnetic Coordination Complexes for Quantum Computing. *Chem. Soc. Rev.* **2012**, *41*, 537−546.

(47) Aguilà, D.; Barrios, L. A.; Velasco, V.; Roubeau, O.; Repollés, A.; Alonso, P. J.; Sesé, J.; Teat, S. J.; Luis, F.; Aromí, G. Heterodimetallic [LnLn'] Lanthanide Complexes: Toward a Chemical Design of Two-Qubit Molecular Spin Quantum Gates. *J. Am. Chem. Soc.* **2014**, *136*, 14215−14222.

(48) Westerström, R.; Dreiser, J.; Piamonteze, C.; Muntwiler, M.; Weyeneth, S.; Brune, H.; Rusponi, S.; Nolting, F.; Popov, A.; Yang, S.; Dunsch, L.; Greber, T. An Endohedral Single-Molecule Magnet with Long Relaxation Times: DySc2N@C80. *J. Am. Chem. Soc.* **2012**, *134*, 9840−9843.

(49) Zadrozny, J. M.; Xiao, D. J.; Atanasov, M.; Long, G. J.; Grandjean, F.; Neese, F.; Long, J. R. Magnetic Blocking in a Linear Iron(I) Complex. *Nat. Chem.* **2013**, *5*, 577−581.

(50) Ungur, L.; Le Roy, J. J.; Korobkov, I.; Murugesu, M.; Chibotaru, L. F. Fine-Tuning the Local Symmetry to Attain Record Blocking Temperature and Magnetic Remanence in a Single-Ion Magnet. *Angew. Chem., Int. Ed.* **2014**, *53*, 4413−4417.

(51) Wäckerlin, C.; Donati, F.; Singha, A.; Baltic, R.; Rusponi, S.; Diller, K.; Patthey, F.; Pivetta, M.; Lan, Y.; Klyatskaya, S.; Ruben, M.; Brune, H.; Dreiser, J. Giant Hysteresis of Single-Molecule Magnets Adsorbed on a Nonmagnetic Insulator. *Adv. Mater.* **2016**, *28*, 5195−5199.

(52) Kouwenhoven, L.; Glazman, L. Revival of the Kondo Effect. *Phys. World* **2001**, *14*, 33.

(53) Nagaoka, K.; Jamneala, T.; Grobis, M.; Crommie, M. F. Temperature Dependence of a Single Kondo Impurity. *Phys. Rev. Lett.* **2002**, *88*, 077205.

(54) Kröger, J.; Limot, L.; Jensen, H.; Berndt, R.; Crampin, S.; Pehlke, E. Surface State Electron Dynamics of Clean and Adsorbate-Covered Metal Surfaces Studied with the Scanning Tunnelling Microscope. *Prog. Surf. Sci.* **2005**, *80*, 26−48.

(55) Schneider, M. A.; Wahl, P.; Diekhöner, L.; Vitali, L.; Wittich, G.; Kern, K. Kondo Effect of Co Adatoms on Ag Monolayers on Noble Metal Surfaces. *JJAP* **2005**, *44*, 5328.

(56) Iancu, V.; Hla, S.-W. Realization of a Four-Step Molecular Switch in Scanning Tunneling Microscope Manipulation of Single Chlorophyll-a Molecules. *Proc. Natl. Acad. Sci. U. S. A.* **2006**, *103*, 13718−13721.

(57) Tierney, H. L.; Murphy, C. J.; Jewell, A. D.; Baber, A. E.; Iski, E. V.; Khodaverdian, H. Y.; McGuire, A. F.; Klebanov, N.; Sykes, E. C. H. Experimental Demonstration of a Single-Molecule Electric Motor. *Nat. Nanotechnol.* **2011**, *6*, 625−629.

(58) Auwärter, W.; Seufert, K.; Bischoff, F.; Ecija, D.; Vijayaraghavan, S.; Joshi, S.; Klappenberger, F.; Samudrala, N.; Barth, J. V. A Surface-Anchored Molecular Four-Level Conductance Switch Based on Single Proton Transfer. *Nat. Nanotechnol.* **2012**, *7*, 41−46.

(59) Perera, U.; Ample, F.; Kersell, H.; Zhang, Y.; Vives, G.; Echeverria, J.; Grisolia, M.; Rapenne, G.; Joachim, C.; Hla, S.-W. Controlled Clockwise and Anticlockwise Rotational Switching of a Molecular Motor. *Nat. Nanotechnol.* **2013**, *8*, 46−51.

(60) Alemani, M.; Peters, M.; Hecht, S.; Rieder, K.-H.; Moresco, F.; Grill, L. Electric Field-Induced Isomerization of Azobenzene by STM. *J. Am. Chem. Soc.* **2006**, *128*, 14446−14447.

(61) Zhang, J. L.; Xu, J. L.; Niu, T. C.; Lu, Y. H.; Liu, L.; Chen, W. Reversible Switching of a Single-Dipole Molecule Imbedded in Two-Dimensional Hydrogen-Bonded Binary Molecular Networks. *J. Phys. Chem. C* **2014**, *118*, 1712−1718.

(62) Parschau, M.; Passerone, D.; Rieder, K.-H.; Hug, H.; Ernst, K.-H. Switching the Chirality of Single Adsorbate Complexes. *Angew. Chem., Int. Ed.* **2009**, *48*, 4065−4068.

(63) Nielsen, M. B.; Diederich, F. Conjugated Oligoenynes Based on the Diethynylethene Unit. *Chem. Rev.* **2005**, *105*, 1837−1867.

(64) Liu, J. Z.; Lam, J. W. Y.; Tang, B. Z. Acetylenic Polymers: Syntheses, Structures, and Functions. *Chem. Rev.* **2009**, *109*, 5799−5867.

(65) Zhang, Y.-Q.; Björk, J.; Barth, J. V.; Klappenberger, F. Intermolecular Hybridization Creating Nanopore Orbital in a Supramolecular Hydrocarbon Sheet. *Nano Lett.* **2016**, *16*, 4274−4281.

(66) Klappenberger, F.; Zhang, Y.-Q.; Björk, J.; Klyatskaya, S.; Ruben, M.; Barth, J. V. On-Surface Synthesis of Carbon-Based Scaffolds and Nanomaterials Using Terminal Alkynes. *Acc. Chem. Res.* **2015**, *48*, 2140−2150.

(67) Dong, L.; Liu, P. N.; Lin, N. Surface-Activated Coupling Reactions Confined on a Surface. *Acc. Chem. Res.* **2015**, *48*, 2765−2774.

(68) Fan, Q. T.; Gottfried, J. M.; Zhu, J. F. Surface-Catalyzed C-C Covalent Coupling Strategies toward the Synthesis of Low-Dimensional Carbon-Based Nanostructures. *Acc. Chem. Res.* **2015**, *48*, 2484−2494.

(69) VandeVondele, J.; Krack, M.; Mohamed, F.; Parrinello, M.; Chassaing, T.; Hutter, J. Quickstep: Fast and Accurate Density Functional Calculations Using a Mixed Gaussian and Plane Waves Approach. *Comput. Phys. Commun.* **2005**, *167*, 103.

(70) *CP2K*; CP2K Foundation: Zürich, Germany, 2015.

(71) Perdew, J. P.; Burke, K.; Ernzerhof, M. Generalized Gradient Approximation Made Simple. *Phys. Rev. Lett.* **1996**, *77*, 3865−3868.

(72) Grimme, S.; Antony, J.; Ehrlich, S.; Krieg, H. A Consistent and Accurate *Ab Initio* Parametrization of Density Functional Dispersion Correction (DFT-D) for the 94 Elements H-Pu. *J. Chem. Phys.* **2010**, *132*, 154104.

(73) Zhang, Y.; Yang, W. Comment on "Generalized Gradient Approximation Made Simple. *Phys. Rev. Lett.* **1998**, *80*, 890.

(74) Lee, K.; Murray, É. D; Kong, L.; Lundqvist, B. I.; Langreth, D. C. Higher-Accuracy van der Waals Density Functional. *Phys. Rev. B: Condens. Matter Mater. Phys.* **2010**, *82*, 081101.

(75) VandeVondele, J.; Hutter, J. Gaussian Basis Sets for Accurate Calculations on Molecular Systems in Gas and Condensed Phases. *J. Chem. Phys.* **2007**, *127*, 114105.

Supporting information for: Epitaxy-Induced Assembly and Enantiomeric Switching of an On-Surface Formed Dinuclear Organocobalt Complex

Raphael Hellwig,[†] Tobias Paintner,[†] Zhi Chen,[‡] Mario Ruben,[‡,¶] Ari Paavo Seitsonen,[§] Florian Klappenberger,[*,†] Harald Brune,[‖,⊥] and Johannes V. Barth[†]

†*Physik Department E20, Technische Universität München, D-85748 Garching, Germany*

‡*Institute of Nanotechnology, Karlsruhe Institute of Technology, D-76344 Eggenstein-Leopoldshafen, Germany*

¶*Institute de Physique et Chimie de Matériaux de Strasbourg (IPCMS), CNRS-Université de Strasbourg, F-67034 Strasbourg, France*

§*Ecole Normale Supérieure (ENS), Département de Chimie, F-75230 Paris Cedex 05, France*

‖*Ecole Polytechnique Fédérale de Lausanne (EPFL), Institute of Physics, Station 3, CH-1015, Switzerland*

⊥*Institute for Advanced Study (TUM-IAS), Lichtenbergstr. 2a, D-85748 Garching, Germany*

E-mail: florian.klappenberger@tum.de

Contents

Details on the chemical synthesis of HEB

^1H nuclear magnetic resonance (NMR) and ^{13}C NMR spectra were recorded on a Bruker DRX 500 spectrometer. Mass data were acquired with a Voyager-DE PRO Bio spectrometry work station for matrix-assisted laser desorption/ionization - time of flight (MALDI-ToF) without additional matrix compound. Elemental analyses were carried out in a Vario Micro Cube. Infrared spectra were measured in KBr pellets (MAGNA FTIR 750, Nicolet) in the 4000-400 cm^{-1} region.

Hexakis((trimethylsilyl)ethynyl)benzene (HEB)^{S1} Hexabromobenzene (0.551 g, 1 mmol), $Pd(PPh_3)_2Cl_2$ (0.070 g, 0.1 mmol) and CuI (0.040 g, 0.2 mmol) were added into the mixture of THF (30 mL) and diisopropylamine (30 mL) under an argon atmosphere. After heating up to 80 °C, 1.1 mL ethynyltrimethylsilane (8 mmol) was added, and then the mixture was stirred at 80 °C for two days (see Figure S1a). Then the solution was poured into 150 mL ammonium chloride aqueous solution and extracted by CH_2Cl_2. Solvents were removed in vacuum and the residue was purified by column chromatography on silica gel (hexane: CH_2Cl_2 = 15:1) twice. The product was further recrystallized from CH_2Cl_2 and hexane gave light yellow cube shape crystals of HEB (0.126 g, yield 19%). ^1H NMR (500 MHz, $CDCl_3$) δ/ppm 0.30 (s). ^{13}C NMR (126 MHz, $CDCl_3$) δ/ppm 127.97, 105.23, 101.00, 0.04. NIR_IR (KBr, cm^{-1}) 2960, 2898, 2157 (C≡C), 1393, 1249, 941, 842, 759, 700, 637, 532, 455. MALDI-ToF calculated for $C_{36}H_{54}Si_6$: $[M^+]$, m/z, 654.3; found, 654.2. Elemental analysis calculated (%) for $C_{36}H_{54}Si_6$: C 65.98, H 8.31; found: C 65.89, H 8.32.

According to gas chromatography-mass spectroscopy (GC-MS) (Figure S1b), defect molecules with five TMS groups exist as byproducts during the synthetic procedure. At the indicated times (red, green, blue outline), individual electron ionization-mass spectroscopy (EI-MS) data were recorded and are shown together with the respective compounds (Figure S1c). After a second column chromatography step and recrystallization, GC-MS only shows the targeted HEB compound (Figure 1d); the corresponding EI-MS is shown in Figure 1e. Also the ^1H- and ^{13}C-NMR spectra shown in Figure S1f,g reveal no impurities.

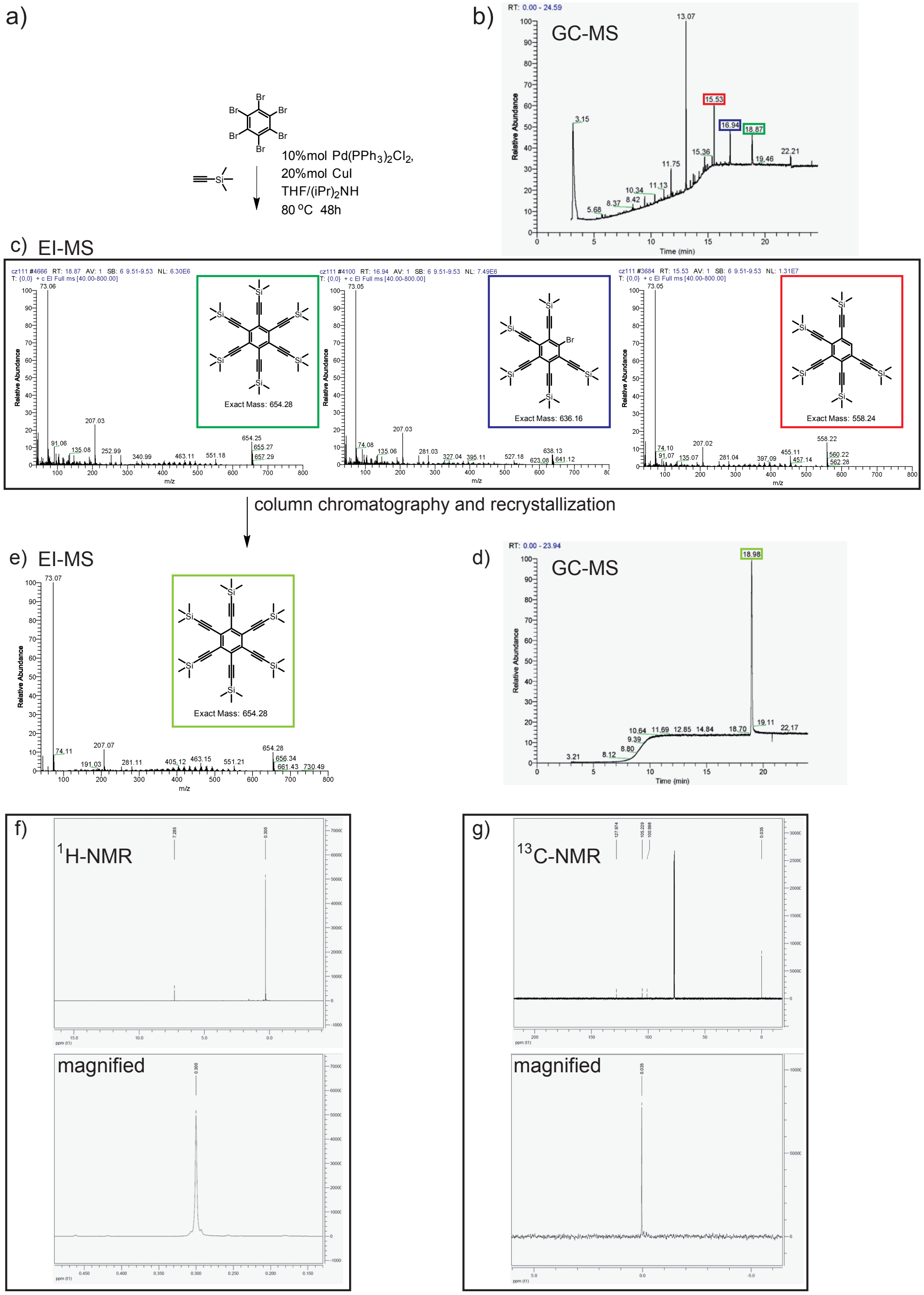

Figure S1: Synthesis route of HEB. (a) First synthesis steps starting from hexabromobenzene. (b) GC-MS spectrum of impurity fractions (red, blue) and HEB (green) after first column chromatography. (c) Corresponding EI-MS spectra of HEB (at the GC time of 18.87 minutes (min)) and impurities at 15.53 and 16.94 min. (d) GC-MS spectrum after second column chromatography and recrystallization. (e) Corresponding EI-MS spectrum of HEB at 18.98 min. (f) ^{1}H NMR spectrum (top) of HEB. Peak at 7.825 stems from solvent ($CDCl_3$), peak at 0.300 stems from $Si(CH_3)_3$ (TMS group). Magnified region of the latter (bottom) does not show any byproducts with five TMS groups. (g) ^{13}C NMR spectrum (top) and magnified region around the peak at 0.035, which is ascribed to $Si(CH_3)_3$ (TMS group). Again, the impurity concentration is too low to be detected.

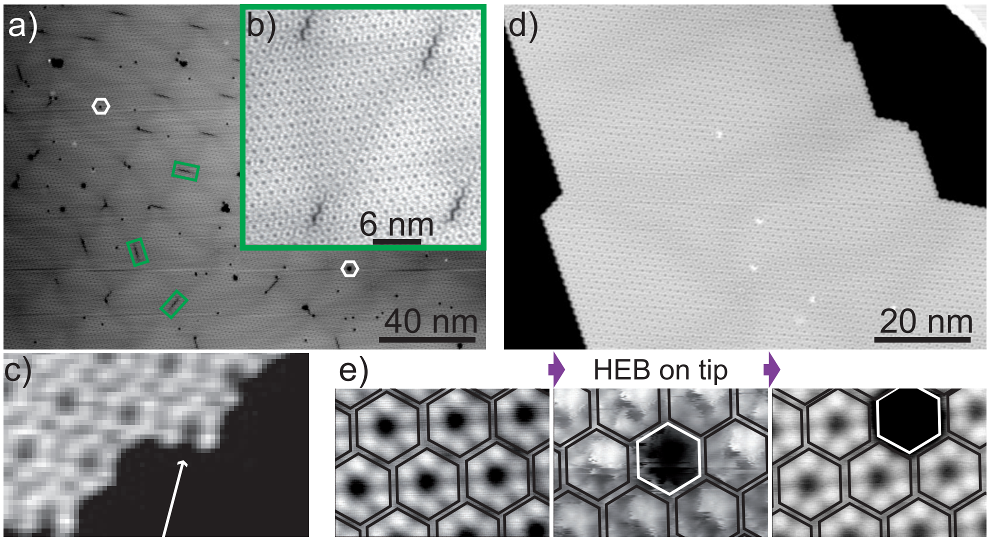

Figure S2: Improving domain morphology through elevated deposition temperature (hot deposition). (a) Molecular deposition at $T \leq 300$ K leads to the presence of structural defects within domains, *i.e.,* vacancies due to missing molecules (white outline), jagged dislocation lines (three 120°-multiple orientations, one of them shown in b)), and a small quantity of defect molecules reflecting five instead of six protrusions (see arrow in c). According to Figure S1c, we rationalize the latter with the absence of one TMS-alkyne group. Since the defect molecules are mainly encountered at island edges, we assume a higher diffusion barrier compared to pristine HEB. Within the domain in a), the reticular structure enclosing triangular-shaped regions in a regular fashion may be regarded as a Moiré-like pattern. Therein, the dislocation lines are often found at the intersection point of three triangles with similar brightness. Since the domains are always comprised of isochiral units, the two triangular regions (dark and bright STM contrast) might be related to regions where all TMS groups are aligned in a certain way, next to regions where all TMS groups are aligned in the opposite way (, but with the same chirality for both sub-domains). (c) STM image with arrow pointing to a defect molecule, which apparently misses one molecular lobe. (d) Hot deposition at 450 K leads to the formation of homogenous domains free of vacancies, dislocation lines, and defect molecules. Since there is no Moiré-like pattern and no dislocation line, we postulate that all molecules within this domain have their TMS groups oriented in a certain way (no triangular sub-domains). Due to the increased thermal energy during the growth process, the highly mobile two-dimensional gas of HEB may condense to a more favorable low-energy structure. From the absence of defect molecules throughout the Ag(111) terraces, we tentatively assume that they either desorbed (due to a smaller molecular weight) or remain bound to step edges (possibly due to reactive sites within the defect molecule). (e) STM tip-induced uptake of an entire molecule *via* a bias pulse (2 V, 1 s). Superimposed hexagonal contours mark molecules. The middle STM image was taken after the bias pulse, by which the scanning tip changed due to the uptake of the marked molecule (white outline). After removing the tip molecule through a tip-sample contact on pristine Ag(111), a rescan of this region (right image) displays initial scanning tip conditions (left image). Tunneling parameters V_t, I_t: (a, d) −1000 mV, 100 pA; (b) −500 mV, 50 pA; (c) −100 mV, 100 pA; (e) 20 mV, 100 pA.

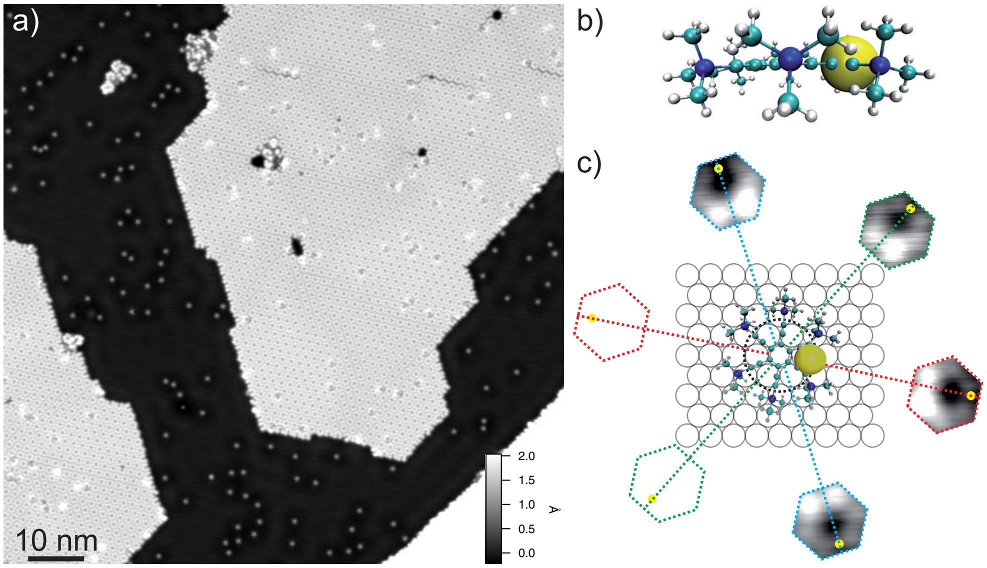

Figure S3: (a) Large-scale STM topography after dosing Co at 12 K on a sample with a sub-ML coverage of HEB molecules. Due to a diffusionless growth of Co, the density of single Co atoms on pristine Ag(111) terraces can be compared with the density of decorated molecules within the islands. Thereby, it is found that each decorated molecule incorporates one Co atom. (b) Side view of a gas-phase DFT model for the monocobalt complex C_1. (c) C_1 complexes embedded in an organic α domain reveal two protruding molecular lobes with different brightness. The brighter lobe indicates its chiral state, classified as 'S' enantiomer. Only four of the six possible orientations are represented by hexagon-shaped sections of STM images. The intersection points between the dashed lines and black circle are located at six hollow sites (other hollow sites and chirality compared to C_1 embedded in a β domain, see manuscript (MS), Figure 2d. Tunneling parameters V_t, I_t: (a) -100 mV, 300 pA; (c) -1000 mV, 50 pA and 100 pA.

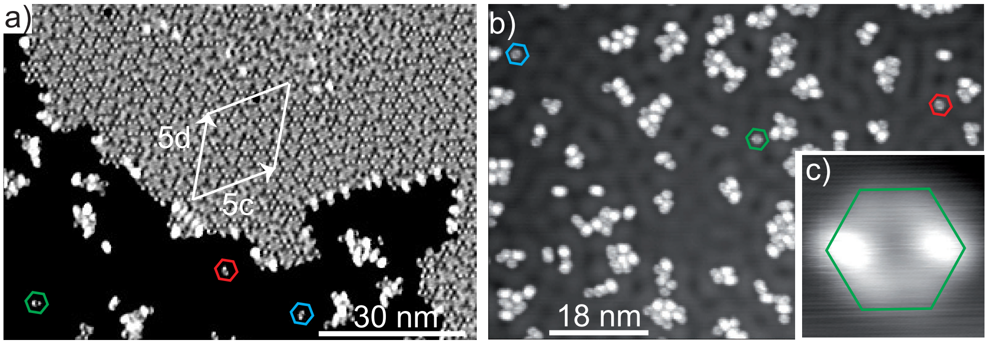

Figure S4: Co deposition at 200 K leads to mono- and dinuclear complexes due to high adsorbate diffusion and low clustering rate. (a) Large-scale STM topograph displaying the organocobalt phase for a high Co/HEB ratio (nominal value 1.23). Isolated C_2 units are spread around the island and marked by color-coded outlines according to their orientation. The white-outlined vectors equal in length to five times the unit cell vectors of the α domain. (b) When preparing a sample with even higher Co-HEB ratio (nominal value 1.85), the 2D domains dissolve, while isolated and intact C_2 complexes remain. Together with the absence of organic islands, the observation of dispersed clusters of molecules irregularly decorated by Co clusters leads us to the conclusion that all remaining pristine HEB molecules converted into complexes and irregular accumulations of Co and HEB. The absence of open-porous honeycomb structures solely comprised of complexes strengthens our interpretation that pristine molecules are necessary to establish the organocobalt phase. Therein, Co-HEB exclusively adsorbs at bridge sites (three MA orientations), while HEB expressing no favored adsorption sites occupies those sites which are unfavorable for Co-HEB. This adsorption behavior explains why condensation toward a dense-packed 2D structures is inhibited at sufficiently high Co-molecule concentrations. (c) Isolated C_2 unit with hexagonal outline. Tunneling parameters V_t, I_t: (a) 100 mV, 100 pA; (b) −10 mV, 100 pA; (c) −10 mV, 50 pA.

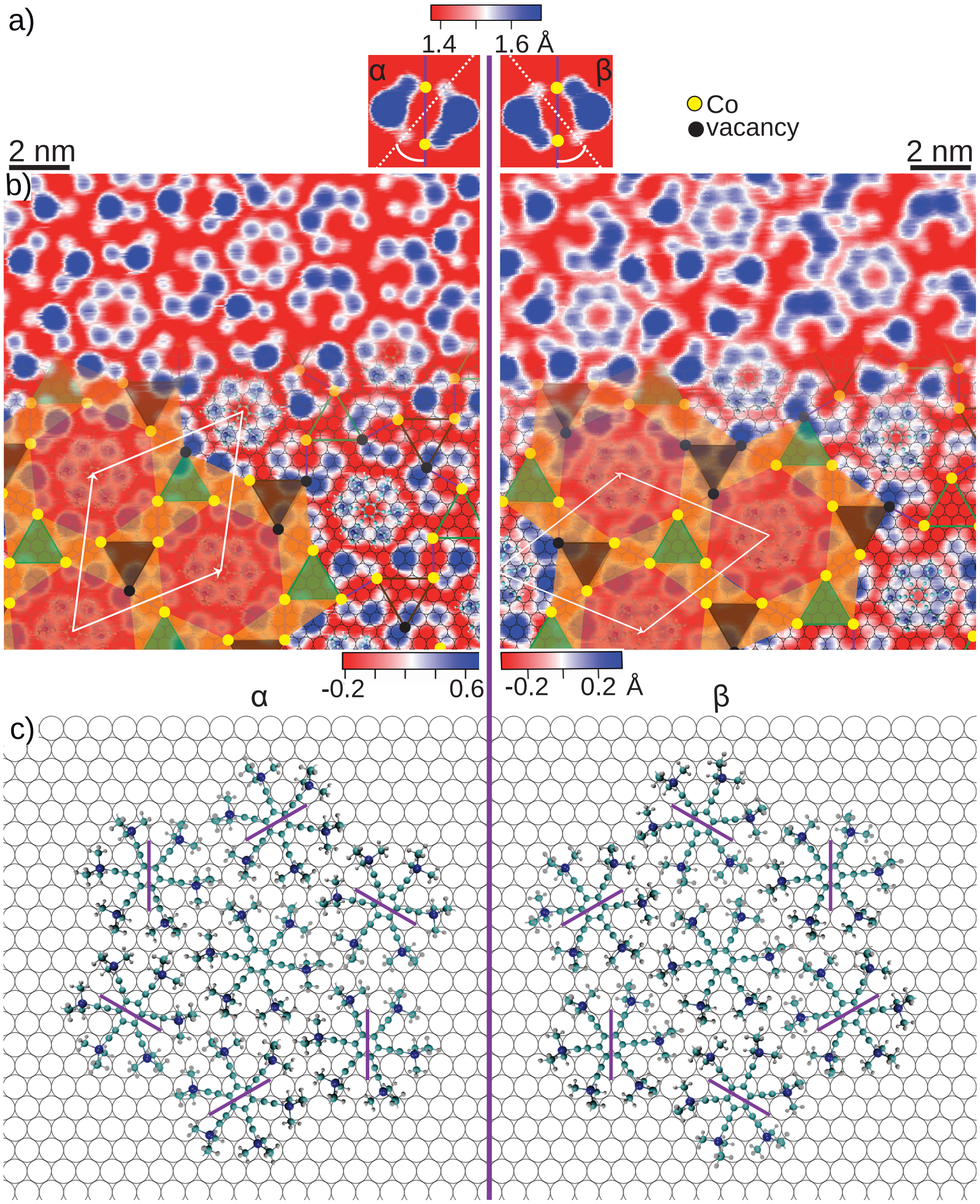

Figure S5: (a) Contrast-enhanced STM results showing two isolated C_2 complexes with same MA, but opposite conformer states (α and β), which are mirror symmetric to their MA (purple line). (b) STM images of the enantiopure α and β organocobalt domain with superimposed Ag(111) lattice and 3.4.6.4 surface tesselation scheme, which is mirror-symmetric to all three MA orientations, *i.e.,* the underlying $\langle 11\overline{2} \rangle$ directions. (c) Atomic Ag(111) lattice model with superimposed HEB models, which are positioned and aligned according to the molecules within the α and β domain in b). For molecules centered at bridge sites, we encounter two opposite hollow sites for Co adsorption, *i.e.,* one fcc and hcp site connected by a purple line (MA). The latter representing the Co-Co axis for each C_2 unit rationalizes the windmill-like motifs (*cf.* MS, Figure 3e) within the surface tesselation pattern in b). Tunneling parameters V_t, I_t: (a) -10 mV, 30 pA; (b) left: -10 mV, 100 pA; right: 20 mV, 100 pA.

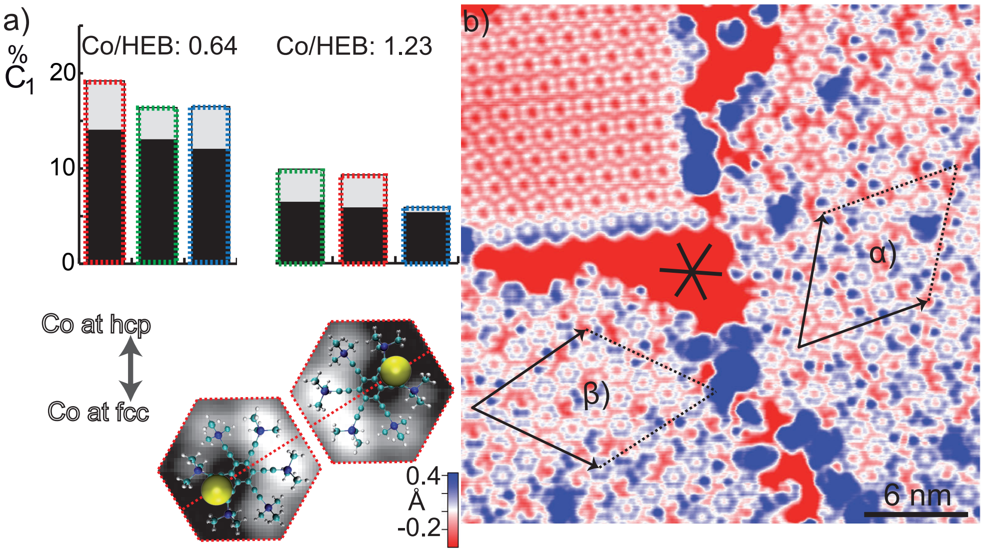

Figure S6: Statistical evaluation of the monocobalt complexes with respect to the binding site of the incorporated Co atom. Since the two Co atoms of C_2 are located close to one fcc and one hcp hollow site of Ag(111), the Co atom of C_1 is expected to adsorb with equal probability close to fcc and hcp sites. (a) Antiparallel alignments of embedded C_1 units with same MA are represented by zooms with superimposed gas-phase DFT models for C_1. According to the statistical evaluation of MS, Figure 3c,f, the shown columns depict the abundance of C_1 with respective MA (colored frame) and are subdivided due to the two antiparallel alignments (black and white area). The left histogram refers to a domain with a Co-molecule ratio of 0.64 (low Co coverage), while the right histogram evaluated a domain with a Co-molecule ratio of 1.23 (high Co coverage). Both histograms clearly show that one alignment of C_1 is preferred for each MA, which implies that the Co atom is preferentially situated at the fcc (hcp) site. (b) Enhanced-contrast STM topograph showing the co-existence of the α and β organocobalt domain within the same Ag(111) terrace. Therefore, we exclude that the imbalance between Co close to hcp and Co close to fcc is related to an alternating atomic arrangement of adjacent atomic Ag(111) planes. Tunneling parameters V_t, I_t: (a) 100 mV, 300 pA; (b) −9 mV, 50 pA.

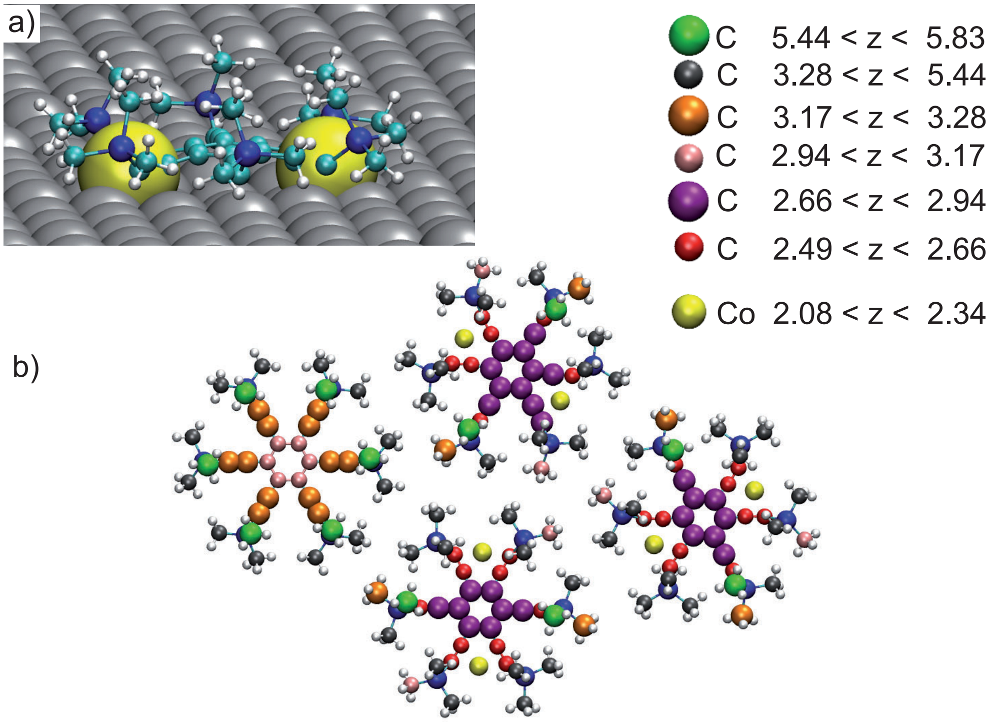

Figure S7: Visualization of DFT-calculated physical heights of all carbon atoms within organocobalt α domain, whereby included Ag(111) surface is only depicted in a) (grey spheres refer to topmost Ag atoms). (a) Side view showing the location of Co atoms and bending of TMS-alkyne moieties. (b) Molecular unit cell with color-coded C atoms according to the labeled z-height intervals. For the C_2 species, C(sp) atoms (red) interacting with Co are preferentially located below the plane of C(sp^2) atoms (purple), while for the pristine molecule, the former (orange) are located above the latter (pink). Since the arene ring of C_2 (purple) is lowered compared to the arene ring of pristine HEB (pink), we conclude that the complexes are pulled downwards *via* underlying Co atoms. Therefore, we conclude a stronger molecule-substrate interaction for C_2 compared to pristine HEB. The positions of the protruding C(sp^3) atoms (green) agree with the STM contrast of the complexes. Diameter of Co atoms is reduced in order to enhance clarity. All numeric values are in Å.

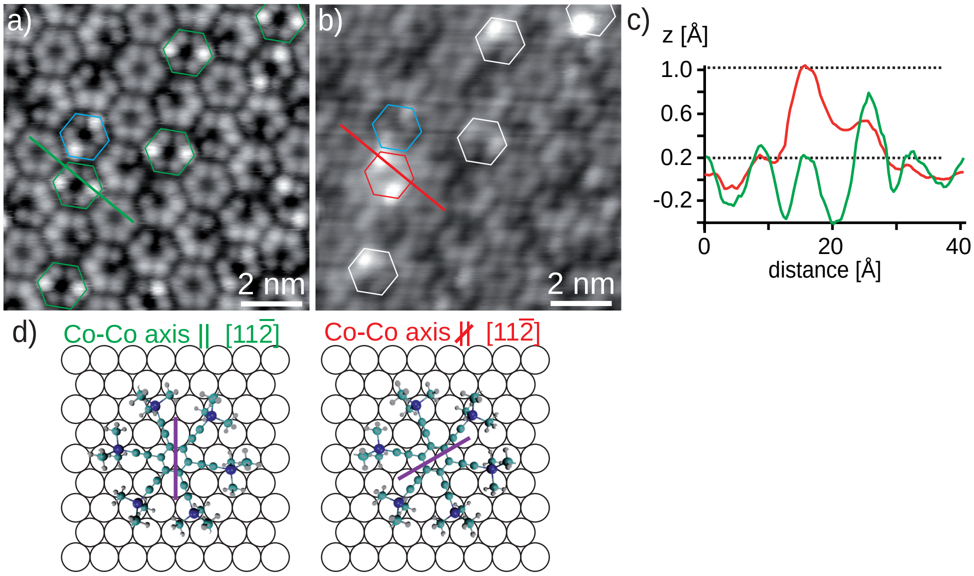

Figure S8: (a) STM image of an organocobalt island prior to the application of one voltage pulse (−2 V, 10 ms) on each of five C_2 units (green hexagonal contours) with same MA. Complex with blue hexagonal contour marks reference point. (b) The subsequent STM image shows structurally modified C_2 units. Remarkably, one C_2 unit underwent a 120°-rotation (red hexagonal countour) and appears with two significantly brighter lobes than the reference point. Apart from the manipulated complexes, the surrounding molecules remain unchanged. (c) Height profiles along the rotated complex (before and after the voltage pulse) indicate a vertical lifting of the entire unit. (d) Left: adsorption model for single C_2 based on aligned HEB model and purple line representing its Co-Co axis connecting one fcc and one hcp hollow site. According to our interpretation, C_2 aligns its Co-Co axis (MA) parallel to the bridge site on which it adsorbed. Right: model after 120°-rotation of C_2 without centering it on a new bridge site parallel to the new MA orientation. This scenario results in unfavorable adsorption sites for the two Co atoms (no deeper lying hollow sites available), and thus lead to the observed lifting of the entire complex. Tunneling parameters V_t, I_t: (a,b) 20 mV, 100 pA.

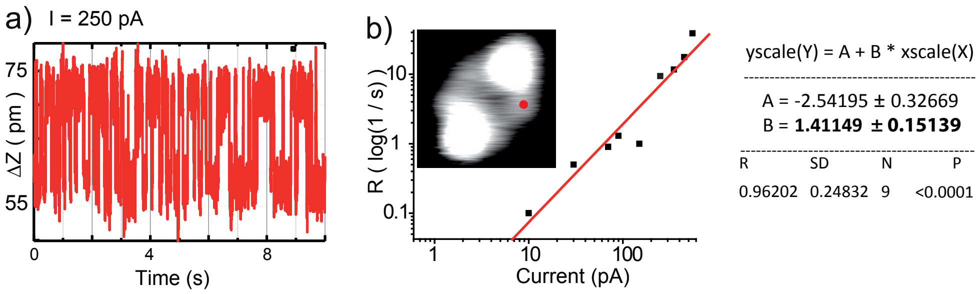

Figure S9: Switching statistic for an isolated C_2 unit with tunneling currents between $I_t = 10$ and 550 pA ($V_t = -40$ mV, $T = 1.2$ K). The tip is positioned on one of the four TMS-alkyne moieties next to Co. (a) Time spectrum showing switching events at $I_t = 250$ pA during a time interval of 10 s (100 μs integration time). (b) Double-logarithmic plot of switching rate *versus* current with associated linear fit delivers a slope parameter B deviating from unity. More statistics is needed to clarify if the switching is dominated by an one-electron process. Tunneling parameters V_t, I_t: (b) -10 mV, 250 pA.

References

(S1) Diercks, R.; Armstrong, J. C.; Boese, R.; Vollhardt, K. P. C. Hexaethynylbenzene. *Angew. Chem., Int. Ed.* **1986**, *25*, 268–269.